A Reduced Particle-in-Cell Model for Two-Plasmon-Decay Instability

Introduction

Two-plasmon-decay (TPD) instability [the parametric decay of a laser (photon) into two Langmuir waves (plasmons)] has recently experienced renewed experimental and theoretical interest, largely based on recent experimental results obtained at the Omega Laser Facility.[1–4] The TPD instability has been the subject of previous theoretical[5,6] and experimental[7] studies. Recent experiments using the OMEGA laser[1] have produced unambiguous evidence that TPD is driven in both spherical and planar targets. The diagnostic evidence includes the simultaneous emission of odd half-harmonic radiation and hard x rays.[1,8] There is also some evidence[2–4] that these hot electrons may be inhibiting the efficient implosion of spherical targets by preheating the core to a higher adiabat.

Although effort has been devoted to the linearized theory of the TPD instability in various regimes,[5,6] it is clear, *a priori*, that a nonlinear theory is necessary to describe its evolution beyond the subpicosecond time to be relevant to experiments. This article is devoted to the development of a new theoretical tool for the study of the nonlinear development of TPD. It describes initial results from the implementation of the reduced particle-in-cell (RPIC) technique to treat the nonlinear evolution of TPD in homogeneous plasmas. The RPIC model is not limited to homogeneous plasma, and future work will include inhomogeneous plasma densities and flow velocities, which are present in experiments. The RPIC modeling and the closely related extended Zakharov (ZAK) modeling[9] are useful tools for studying the nonlinear regimes of parametric instabilities. The RPIC and ZAK models have been previously applied to the nonlinear development of stimulated Raman scattering (SRS)[10] and to the nonlinear development of the parametric decay instability (PDI).[11] In these studies, nonlinear processes such as the Langmuir decay instability (LDI) [the parametric decay of a Langmuir wave (LW) into another LW and an ion-acoustic wave (IAW)], Langmuir cavitation, and electron trapping have been observed to compete. Several predictions of this modeling have been experimentally verified.[12]

The RPIC model, while fully kinetic in regards to both electron and ion dynamics, shares certain features with the reduced, fluid-like ZAK modeling.[13] Both models represent the transverse fields, longitudinal fields, and density fields in terms of slowly varying envelopes of rapidly oscillating phase factors. This approach assumes a well-defined separation of time scales between the laser, LW, and IAW oscillations. This representation of field quantities stands in contrast with the standard particle-in-cell (PIC) technique in which the full-time variations are followed explicitly.[14] In **Appendix B** (p. 103), a derivation of the extended Zakharov model directly from the RPIC equations of motion is presented. This derivation provides a direct theoretical connection between the kinetic RPIC and the fluid-like ZAK models. Furthermore, such a theoretical connection provides guidance on how one should proceed with *quantitative* comparison of the two models.

In the RPIC simulations, unique signatures of LDI are found that are suggestive of LDI as one of the primary saturation processes. Spectral signatures of LDI processes are strikingly similar, at least semi-quantitatively, to those found from ZAK modeling. In addition, the RPIC model also predicts heated-electron velocity distributions in the quasi-stationary nonlinear regime. Previous RPIC modeling has been extremely successful in modeling the nonlinear behavior of parametric instabilities involving the Langmuir decay instability, largely because RPIC eliminates the often unphysically high electron–ion collision rate present in explicit PIC codes, while at the same time allowing for the use of a modest number of simulation particles per simulation cell. For instance, for a plasma in quasi-thermodynamic equilibrium with $T_\mathrm{e}/T_\mathrm{i} \gg 1$, RPIC will preserve the temperature ratio perfectly over an extended time, whereas in standard PIC codes, this ratio will become unity prematurely because of the unphysically rapid electron–ion energy equilibration rate.[15] This is problematic when ion modes are involved, such as in LDI, since the IAW damping rate is sensitive to this ratio (cf. Ref. 16). Additional effects expected from the strong electron–ion collisions (even when $T_{\mathrm{e}0} = T_{\mathrm{i}0}$) include unphysically large collisional damping of LW's and IAW's. Elimination of unphysical electron–ion collisions makes it possible for RPIC simulations to operate with fewer particles per simulation cell than standard PIC codes. It is important to observe that the earliest application of PIC codes to TPD by Langdon *et al.*[5] and more recently by Yan *et al.*[14] observed a high level of ion-density fluctuations. It is not clear in retrospect that these can be interpreted as resulting from IAW fluctuations excited by LDI as found in this work.

In previous work using ZAK modeling[9] it was found, among other things, that LDI produces a distinct, rich Fourier spectrum of electron- and ion-density fluctuations. Furthermore, this modeling provided an explanation for the well-known problem that the primary, i.e., most linearly unstable, TPD Langmuir waves cannot couple locally to the (observed) radiation at $3\omega_0/2$, where ω_0 is the laser frequency. In Russell *et al.*,[17] it was shown that there is an efficient local coupling of the secondary LDI-produced LW's to the $3\omega_0/2$ emission and this coupling in turn produced, in an inhomogeneous plasma, a distinctive double-peaked $3\omega_0/2$ frequency spectrum. RPIC has the advantage that the envelope fields can be used directly to compute the currents for the $3\omega_0/2$ radiation, as was done in Russell *et al.*[17] and also more recently for the $\omega_0/2$ radiation current as shown in DuBois *et al.*[18] The latter application of RPIC to $\omega_0/2$ radiation is proposed for future work.

The article is organized as follows: (1) The equations for the physical model underlying RPIC are discussed. This involves expressing the electromagnetic vector potential, the longitudinal scalar potential, and the plasma density in temporal envelope representations (the primary objective of the RPIC formulation is to eliminate the laser time scale from the electron equation of motion and the laser and LW time scales from the ion equation of motion). (2) A sketch of the derivation of the RPIC model for TPD is given, with the details provided in **Appendix A**, p. 101. An important element in this derivation (as in previous implementations of RPIC[15]) is the closure of the model set of equations with an auxiliary electron equation of state. (3) Results of both RPIC and ZAK simulations of TPD in a homogeneous plasma are presented (including the standard problem of a single coherent laser beam) along with simulations of oblique overlapped beams propagating at angles of ±23° relative to the *x* axis common in OMEGA geometry.[1] Finally, a summary and conclusions are presented.

Physical Model

The vector potential, scalar potential, and electron density are written as[19]

$$\mathbf{A}(\mathbf{x},t)=\frac{1}{2}\left[\mathbf{a}_0\exp\left(-i\omega_0 t\right)+\text{c.c.}\right], \tag{1}$$

$$\phi(\mathbf{x},t)=\phi_S+\frac{1}{2}\left[\phi_F\exp\left(-i\omega_{\text{LW}}t\right)+\text{c.c.}\right], \tag{2}$$

$$n(\mathbf{x},t)=n_S+\frac{1}{2}\left[n_F\exp\left(-i\omega_{\text{LW}}t\right)+\text{c.c.}\right], \tag{3}$$

where ω_0 is the laser frequency and ω_{LW} is the carrier frequency of the LW density and electric-field perturbations. In the RPIC model, ω_{LW} is an input parameter and is typically chosen to be $\omega_{\text{LW}}=\omega_{\text{pe0}}$ (where $\omega_{\text{pe0}}^2=4\pi e^2 n_{\text{e0}}/m_{\text{e}}$), e is the unsigned electronic charge, n_{e0} is the electron number density, and m_{e} is the mass of an electron. The subscripts S and F refer to the slow (ion-acoustic wave and profile modification) and fast (Langmuir wave) time scales, respectively. It is assumed that the density is at, or near, quarter-critical density so that $\omega_0\approx 2\omega_{\text{LW}}$. The model is also restricted to two spatial dimensions (x,y), with z the ignorable coordinate.

The goal of the RPIC formulation is to eliminate the laser time scale from the electron equations of motion and the laser and Langmuir wave time scales from the ion equations of motion. The particle velocities and positions in RPIC, by necessity, are measured in an oscillating and, therefore, noninertial frame.

1. Single-Particle Equation in an Oscillating Frame

The nonrelativistic equation of motion for the single-particle velocity $\mathbf{u}\left[=u_x(x,y)\hat{\mathbf{x}}+u_y(x,y)\hat{\mathbf{y}}\right]$ is given by

$$m\frac{\mathrm{d}\mathbf{u}}{\mathrm{d}t}=q\left(-\nabla\phi-\frac{1}{c}\frac{\partial\mathbf{A}}{\partial t}+\frac{\mathbf{u}\times\nabla\times\mathbf{A}}{c}\right). \tag{4}$$

Rewriting the above equation with the change of variable $\mathbf{u}\equiv\tilde{\mathbf{u}}-q\mathbf{A}/mc$, one obtains

$$m\left(\frac{\mathrm{d}\tilde{\mathbf{u}}}{\mathrm{d}t}-\frac{q}{mc}\frac{\partial\mathbf{A}}{\partial t}-\frac{q}{mc}\mathbf{u}\cdot\nabla\mathbf{A}\right)$$

$$=q\left(-\nabla\phi-\frac{1}{c}\frac{\partial\mathbf{A}}{\partial t}+\frac{\mathbf{u}\times\nabla\times\mathbf{A}}{c}\right) \tag{5a}$$

and

$$m\frac{\mathrm{d}\tilde{\mathbf{u}}}{\mathrm{d}t}=-\nabla\left(q\phi+\frac{q^2}{2mc^2}\mathbf{A}\cdot\mathbf{A}\right)$$

$$+\frac{q}{c}\left(\tilde{\mathbf{u}}\times\nabla\times\mathbf{A}+\tilde{\mathbf{u}}\cdot\nabla\mathbf{A}\right). \tag{5b}$$

Note that the operators ∇ and d/dt in the above equation are measured in the laboratory frame. The above equation can be written in the oscillating frame $(\tilde{\mathbf{x}},\tilde{t})$, which moves with velocity $-q\mathbf{A}/mc$ relative to the lab frame $(\mathbf{x},t)$ by using the following coordinate transformation:

$$\mathbf{u} = \tilde{\mathbf{u}} - \frac{q\mathbf{A}(\mathbf{x},t)}{mc}, \tag{6}$$

$$\mathbf{x} = \tilde{\mathbf{x}} - \frac{q}{mc}\int_0^t \mathbf{A}\left[\mathbf{x}(\tau),\tau\right]\mathrm{d}\tau, \tag{7}$$

$$t = \tilde{t}. \tag{8}$$

The various partial derivatives required for the transformation $(\mathbf{x},t) \rightarrow (\tilde{\mathbf{x}},\tilde{t})$ are

$$\frac{\partial\tilde{t}}{\partial t} = 1, \tag{9}$$

$$\frac{\partial\tilde{t}}{\partial\mathbf{x}} = 0, \tag{10}$$

$$\frac{\partial\tilde{\mathbf{x}}}{\partial t} = \frac{q\mathbf{A}}{mc}, \tag{11}$$

$$\frac{\partial\tilde{\mathbf{x}}}{\partial\mathbf{x}} = \mathbf{I}. \tag{12}$$

By using the chain rule and the partial derivatives shown above, one obtains

$$\frac{\partial}{\partial t} = \frac{\partial\tilde{t}}{\partial t}\frac{\partial}{\partial\tilde{t}} + \frac{\partial\tilde{\mathbf{x}}}{\partial t}\cdot\frac{\partial}{\partial\tilde{\mathbf{x}}} = \frac{\partial}{\partial\tilde{t}} + \frac{q\mathbf{A}}{mc}\cdot\frac{\partial}{\partial\tilde{\mathbf{x}}}, \tag{13}$$

$$\frac{\partial}{\partial\mathbf{x}} = \frac{\partial\tilde{t}}{\partial\mathbf{x}}\frac{\partial}{\partial\tilde{t}} + \frac{\partial\tilde{\mathbf{x}}}{\partial\mathbf{x}}\cdot\frac{\partial}{\partial\tilde{\mathbf{x}}} = \frac{\partial}{\partial\tilde{\mathbf{x}}}. \tag{14}$$

The transformation from $(\mathbf{x},t)$ to $(\tilde{\mathbf{x}},\tilde{t})$ proceeds as

$$\begin{aligned}\frac{\mathrm{d}}{\mathrm{d}t} &= \frac{\partial}{\partial t} + \mathbf{u}\cdot\frac{\partial}{\partial\mathbf{x}},\\ &= \frac{\partial}{\partial\tilde{t}} + \frac{q\mathbf{A}}{mc}\cdot\frac{\partial}{\partial\tilde{\mathbf{x}}} + \mathbf{u}\cdot\frac{\partial}{\partial\tilde{\mathbf{x}}},\\ &= \frac{\partial}{\partial\tilde{t}} + \tilde{\mathbf{u}}\cdot\frac{\partial}{\partial\tilde{\mathbf{x}}},\\ \frac{\mathrm{d}}{\mathrm{d}t} &= \frac{\mathrm{d}}{\mathrm{d}\tilde{t}}.\end{aligned} \tag{15}$$

Equation (5) can now be rewritten as

$$m\frac{\mathrm{d}\tilde{\mathbf{u}}}{\mathrm{d}\tilde{t}} = -\tilde{\nabla}\left(q\phi + \frac{q^2}{2mc^2}\mathbf{A}\cdot\mathbf{A}\right) + \frac{q}{c}\left[\tilde{\nabla}(\tilde{\mathbf{u}}\cdot\mathbf{A}) - \mathbf{A}\times\tilde{\nabla}\times\tilde{\mathbf{u}} - \mathbf{A}\cdot\tilde{\nabla}\tilde{\mathbf{u}}\right], \tag{16}$$

$$\frac{\mathrm{d}\tilde{\mathbf{x}}}{\mathrm{d}\tilde{t}} = \tilde{\mathbf{u}}, \tag{17}$$

where the vector identity

$$\tilde{\nabla}(\tilde{\mathbf{u}}\cdot\mathbf{A}) = \tilde{\mathbf{u}}\times\tilde{\nabla}\times\mathbf{A} + \mathbf{A}\times\tilde{\nabla}\times\tilde{\mathbf{u}} + \mathbf{A}\cdot\tilde{\nabla}\tilde{\mathbf{u}} + \tilde{\mathbf{u}}\cdot\tilde{\nabla}\mathbf{A}$$

has been used. Note that Eqs. (16) and (17), which are valid for both electrons and ions, are exact.

2. Fluid Equations

The electron fluid momentum equation is obtained by integrating Eq. (16) (the single-particle equation of motion) over the distribution function, writing explicitly $\mathrm{d}/\mathrm{d}\tilde{t} \equiv \partial/\partial\tilde{t} + \tilde{\mathbf{U}}\cdot\tilde{\nabla}$,

$$mn\left(\frac{\partial\tilde{\mathbf{U}}}{\partial\tilde{t}} + \tilde{\mathbf{U}}\cdot\tilde{\nabla}\tilde{\mathbf{U}}\right) = -n\tilde{\nabla}\left(q\phi + \frac{q^2}{2mc^2}\mathbf{A}\cdot\mathbf{A}\right) + \frac{qn}{c}\left[\tilde{\nabla}(\tilde{\mathbf{U}}\cdot\mathbf{A}) - \mathbf{A}\times\tilde{\nabla}\times\tilde{\mathbf{U}} - \mathbf{A}\cdot\tilde{\nabla}\tilde{\mathbf{U}}\right] - \tilde{\nabla}p, \tag{18}$$

where n, $\tilde{\mathbf{U}}$, and p are the electron density, fluid velocity, and fluid pressure in the oscillating frame. For an isotropic background electron-velocity distribution f,

$$n \equiv \int f(|\tilde{\mathbf{u}}|)\mathrm{d}^3\tilde{\mathbf{u}}\,,$$

$$n\tilde{\mathbf{U}} \equiv \int \tilde{\mathbf{u}} f(|\tilde{\mathbf{u}}|)\mathrm{d}^3\tilde{\mathbf{u}}\,,$$

$$p \equiv \int m|\tilde{\mathbf{u}} - \tilde{\mathbf{U}}|^2 f(|\tilde{\mathbf{u}}|)\mathrm{d}^3\tilde{\mathbf{u}}\,.$$

In the special case of an isotropic Maxwellian distribution function, $p = n_\mathrm{e}T_\mathrm{e}$.

The RPIC Model

The derivation of the RPIC model for TPD can be divided into three separate tasks: First, the fluid momentum equation [Eq. (18)] is averaged over the fast laser time scale to derive an electron equation of state, which itself provides closure for the RPIC model. Second, Eq. (18) is also used to derive the transverse electron current, which provides the driving sources in the nonlinear Schrödinger equation for the incident EM waves. Third, the single-particle equation [Eq. (16)] is averaged over the fast laser time scale to derive a reduced-description, single-particle equation of motion (only a summary of the RPIC model is given below; detailed derivations of these equations can be found in **Appendix A**, p. 101).

The electrons are advanced using the following reduced-description equations of motion:

$$m_\mathrm{e}\frac{\mathrm{d}\tilde{\mathbf{u}}_\mathrm{e}}{\mathrm{d}\tilde{t}} \approx -e\mathbf{E} - \frac{e^2}{4m_\mathrm{e}c^2}\tilde{\nabla}\left|\mathbf{a}_0\right|^2$$

$$-\frac{e^2}{4cm_\mathrm{e}\omega_\mathrm{LW}}\left\{i\tilde{\nabla}\left(\mathbf{E}_F^*\cdot\mathbf{a}_0\right)\exp\left[-i\left(\omega_0-\omega_\mathrm{LW}\right)\tilde{t}\right]+\mathrm{c.c.}\right\}$$

$$-\frac{e^2}{4cm_\mathrm{e}\omega_\mathrm{LW}}\left\{-i\left(\mathbf{a}_0\cdot\tilde{\nabla}\right)\mathbf{E}_F^*\exp\left[-i\left(\omega_0-\omega_\mathrm{LW}\right)\tilde{t}\right]+\mathrm{c.c.}\right\}, \quad (19)$$

$$\frac{\mathrm{d}\tilde{\mathbf{x}}_\mathrm{e}}{\mathrm{d}\tilde{t}} = \tilde{\mathbf{u}}_\mathrm{e}\,,$$

$$\mathbf{E} \equiv -\tilde{\nabla}\phi\,, \quad (20)$$

$$\mathbf{E}_F \equiv -\tilde{\nabla}\phi_F\,,$$

and the ions by

$$m_\mathrm{i}\frac{\mathrm{d}\tilde{\mathbf{u}}_\mathrm{i}}{\mathrm{d}\tilde{t}} = Z_\mathrm{i}e\mathbf{E}_S - \frac{Z^2e^2}{4m_\mathrm{i}c^2}\tilde{\nabla}\left|\mathbf{a}_0\right|^2,$$

$$\frac{\mathrm{d}\tilde{\mathbf{x}}_\mathrm{i}}{\mathrm{d}\tilde{t}} = \tilde{\mathbf{u}}_\mathrm{i}\,,$$

$$\mathbf{E}_S \equiv -\tilde{\nabla}\phi_S\,. \quad (21)$$

Here, Z_i and m_i are the ion charge state and ion mass, respectively. The electron and ion charge densities are interpolated from the particle data onto the computational mesh:

$$-en_\mathrm{e}(\tilde{\mathbf{x}},\tilde{t}) = \sum_{\mathrm{p}\in\mathrm{e}} q_pS\left[\tilde{\mathbf{x}}-\tilde{\mathbf{x}}_p(\tilde{t})\right], \quad (22)$$

$$eZ_\mathrm{i}n_\mathrm{i}(\tilde{\mathbf{x}},\tilde{t}) = \sum_{\mathrm{p}\in\mathrm{i}} q_pS\left[\tilde{\mathbf{x}}-\tilde{\mathbf{x}}_p(\tilde{t})\right]. \quad (23)$$

The particle shape function $S(\mathbf{x})$ is the bi-quadratic B-spline of compact supports Δx and Δy (Δx and Δy are the discrete grid spacings of the computational mesh).[15] The symbols $\Sigma_{\mathrm{p}\in\mathrm{e}}$ and $\Sigma_{\mathrm{p}\in\mathrm{i}}$ denote summations over the finite-size electron particles and finite-size ion particles, respectively. The electrostatic potentials ϕ, ϕ_S, and ϕ_F are obtained by solving the Poisson equation in conjunction with the auxiliary electron equation of state:

$$\tilde{\nabla}^2\phi = 4\pi e\left(n_\mathrm{e} - \sum_\mathrm{i} Z_\mathrm{i}n_\mathrm{i}\right), \quad (24)$$

$$\tilde{\nabla}^2\phi_S = 4\pi e\left(n_{\mathrm{e}S} - \sum_\mathrm{i} Z_\mathrm{i}n_\mathrm{i}\right), \quad (25)$$

$$\alpha(t) = e\phi_S - \frac{e^2}{4m_\mathrm{e}\omega_\mathrm{LW}^2}\left|\mathbf{E}_\mathrm{eff}\right|^2 - \frac{e^2}{4m_\mathrm{e}^2c^2}\left|\mathbf{a}_0\right|^2 - f\left(\gamma,n_{\mathrm{e}S}\right), \quad (26)$$

where

$$f\left(\gamma,n_{\mathrm{e}S}\right) = \begin{cases} T_{\mathrm{e}0}\ln\left(n_{\mathrm{e}S}/n_{\mathrm{e}0}\right) & \text{for } \gamma = 1, \\ T_{\mathrm{e}0}\left(\dfrac{\gamma}{\gamma-1}\right)\left(n_{\mathrm{e}S}/n_{\mathrm{e}0}\right)^{\gamma-1} & \text{otherwise}\,. \end{cases} \quad (27)$$

$$\mathbf{E}_{\text{eff}} \equiv \mathbf{E}_F - \frac{e}{2im_{\text{e}}c\omega_{\text{LW}}}\exp(-i\Delta\omega\tilde{t})\Big[\tilde{\nabla}\left(\mathbf{E}_F^{*}\cdot\mathbf{a}_0\right) + \mathbf{a}_0\cdot\tilde{\nabla}\mathbf{E}_F^{*}\Big], \tag{28}$$

$$\phi_F \approx \exp\left(i\omega_{\text{LW}}\tilde{t}\right)\left[-\frac{1}{i\omega_{\text{LW}}}\frac{\partial\phi}{\partial\tilde{t}} + \left(\phi-\phi_S\right)\right], \tag{29}$$

$$\Delta\omega \equiv \omega_0 - 2\omega_{\text{LW}}. \tag{30}$$

Here, α is the constant of integration chosen to satisfy global charge conservation and γ is the ratio of specific heats (isothermal electrons: γ = 1; adiabatic electrons: γ = 5/3), and $n_{\text{e}0}$ is the background electron number density. Finally, the incident EM field is advanced self-consistently in time by solving the nonlinear Schrödinger equation

$$i\left(\frac{2\omega_0}{c^2}\right)\frac{\partial\mathbf{a}_0}{\partial\tilde{t}} + \tilde{\nabla}^2\mathbf{a}_0 + \frac{1}{c^2}\left(\omega_0^2 - \frac{4\pi e^2 n_S}{m_{\text{e}}}\right)\mathbf{a}_0 = -\frac{4\pi}{c}\tilde{\nabla}\chi_0 + \frac{4\pi e^2 n_{\text{e}F}}{2im_{\text{e}}c\omega_{\text{LW}}}\tilde{\mathbf{E}}_{\text{eff}}\exp(i\Delta\omega\tilde{t}), \tag{31}$$

where

$$\nabla^2\chi_0 = -\nabla\cdot\mathbf{J}_0, \tag{32}$$

$$\mathbf{J}_0 = -\frac{e^2 n_{\text{e}S}\mathbf{a}_0}{m_{\text{e}}c} - \frac{e^2 n_{\text{e}F}}{2im_{\text{e}}\omega_{\text{LW}}}\mathbf{E}_{\text{eff}}\exp(i\Delta\omega\tilde{t}). \tag{33}$$

The projection operator in Eq. (32) ensures that the gauge condition $\nabla\cdot\mathbf{a}_0 = 0$ is preserved.

Equations (19)–(33) are solved self-consistently on a rectangular simulation domain with $0 \le x \le x_{\max}$ and $0 \le y \le y_{\max}$, consisting of $N_x \times N_y$ computational cells of equal size. The EM wave of the laser is permitted to propagate along an arbitrary direction in the x–y plane and is linearly polarized (normal to the direction of wave propagation). The field boundary conditions are periodic in the y direction but are aperiodic in the x direction with $\phi(x=0,y) = \phi(x=x_{\max},y) = 0$. At all boundary surfaces, i.e., $x=0$, $x=x_{\max}$, $y=0$, and $y=y_{\max}$, particles leaving the domain are absorbed (removed), and new particles are injected consistent with a Maxwellian bath (with a temperature given by the plasma's initial state) surrounding the simulation domain (see Fig. 122.25). Modification of the particle boundary conditions (for example, to account for recirculation of hot electrons[20]) is an important problem for future research, as discussed in **Summary and Conclusions** (p. 101). Finally, the RPIC code is fully parallel, based on the Message Passing Interface (MPI),[15] and has a number of built-in spectral, hot-electron, and spatial diagnostics.

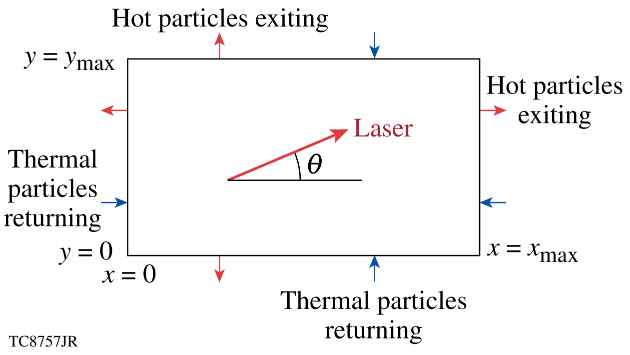

Figure 122.25
The two-dimensional simulation geometry. A Maxwellian bath of electrons at temperature $T_{\text{e}0}$ is assumed to surround the rectangular simulation domain. The laser light can be specified as multiple plane-wave sources, propagating at arbitrary angles θ to the x direction.

Simulation Results

Three sets of simulations are presented in this section. For each set, two simulations were performed with identical parameters on the domain $x_{\max}$ = 20 μm, $y_{\max}$ = 10 μm, and consisting of $N_x \times N_y = 2048 \times 1024$ computational cells of equal size (see Fig. 122.25). In all cases the incident laser light had a vacuum wavelength of $\lambda_0 = 0.351$ μm and the plasma was fully ionized hydrogen (Z = 1). The two simulations highlight the qualitative similarities and quantitative differences between the kinetic RPIC model [Eqs. (19)–(33)] and its (fluid) limiting form that has been derived in Appendix B [Eqs. (B40)–(B41)]. The limiting form, given by Eqs. (B40)–(B41), is solved using the existing extended-Zakharov code "ZAK," which is described in DuBois *et al.*[9] The equations solved by ZAK are advanced in time using split steps: spatial gradients are computed in configuration space, and Landau damping of LW's and IAW's, which are k dependent, are computed in Fourier space. These results, which are by no means exhaustive, are presented to illustrate the utility and capability of the RPIC code and to motivate further studies.

The first simulation set investigated the decay of a single-plane electromagnetic (EM) wave propagating in the positive x direction. Pump depletion was not considered, i.e., $\mathbf{a}_0 = a_{00}\hat{\mathbf{y}}\exp\left(ik_0x\right)$, where a_{00} is a constant [Eq. (31) is not solved]. The pump laser had an intensity of $I_0 = 2 \times 10^{15}$ W/cm^2, corresponding to a linear (amplitude) growth rate of $\gamma_{\text{TPD}}/\omega_{\text{pe0}} \simeq 6.4\times10^{-3}$, which is 50× above the collisional threshold (the collision frequency $\nu_{\text{e0}}/\omega_{\text{pe0}}$ was taken to be $\sim 9.1 \times 10^{-4}$). The plasma was of uniform initial density $n_{\text{e0}}/n_{\text{c}} = 0.23$ [where $n_{\text{c}} = m_{\text{e}}\omega_0^2/\left(4\pi e^2\right)$ is the critical density] and the electron- and ion-plasma temperatures were $T_{\text{e0}} =$ 4 keV and $T_{\text{i0}} = 2$ keV, respectively. This electron temperature was about a factor of 2 higher than typically found in OMEGA experiments and was chosen because the spectral components (e.g., due to LDI) were more widely separated because of the large value of $k\lambda_{\text{De}}$, where $\lambda_{\text{De}} \equiv v_{\text{the}}/\omega_{\text{pe0}}$ is the electron Debye length and $v_{\text{the}} \equiv \left(T_{\text{e0}}/m_{\text{e}}\right)^{1/2}$ is the electron thermal speed. The electrons and ions were each represented by 16 particles per computational cell. The discrete time step was $\omega_{\text{pe0}}\Delta t = 0.1$ or, alternatively, $\Delta t \approx 3.88 \times 10^{-5}$ ps.

Figure 122.26 shows, from strictly linear-fluid considerations, the locations of frequency- and wave-number–matched LW's (circle),

$$\left(k_x\lambda_{\text{De}} - \frac{1}{2}k_0\lambda_{\text{De}}\right)^2 + \left(k_y\lambda_{\text{De}}\right)^2 = \kappa^2, \qquad (34)$$

and the locations of maximum TPD growth (hyperbola),

$$\left(k_x\lambda_{\text{De}} - \frac{1}{2}k_0\lambda_{\text{De}}\right)^2 - \left(k_y\lambda_{\text{De}}\right)^2 = \left(\frac{1}{2}k_0\lambda_{\text{De}}\right)^2. \qquad (35)$$

Here κ is defined as

$$\kappa \equiv \sqrt{\frac{1}{2}\Omega - \left(\frac{1}{2}k_0\lambda_{\text{De}}\right)^2}, \text{ with } \Omega \equiv \frac{2}{3}\left(\frac{\omega_0}{\omega_{\text{pe0}}} - 2\right), \qquad (36)$$

and $k_0 = \omega_0/c\sqrt{1 - n_{\text{e0}}/n_{\text{c}}}$ is the laser light's wave number in the plasma. The intersections of the circle and the hyperbola are locations where TPD-produced LW's are expected to be the most intense. In Fig. 122.26, the two linear modes indicated by the label "1" and located at

$$\mathbf{k}\lambda_{\text{De}}\left[\equiv \left(k_x\lambda_{\text{De}}, k_y\lambda_{\text{De}}\right)\right] = (0.20, \pm0.087)$$

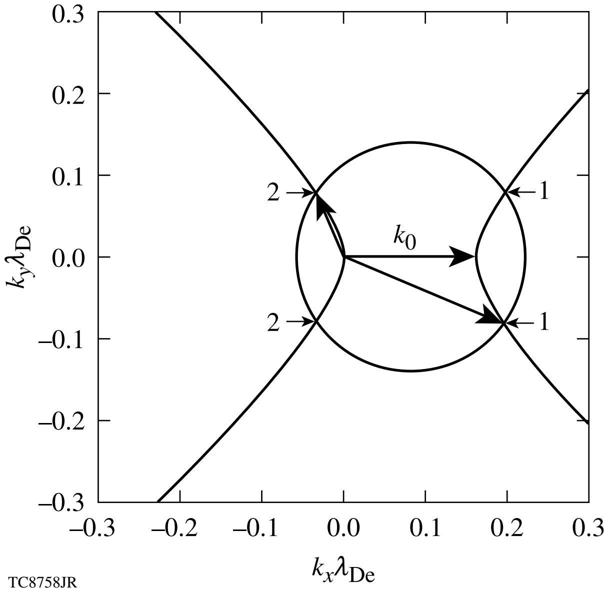

Figure 122.26
The expected wave numbers for plasmons occurring in the TPD instability of a single pump laser propagating in the x direction with parameters $T_{\text{e0}} =$ 4 keV and $n_{\text{e}}/n_{\text{c}} = 0.23$. The circle represents all possible wave-number- and frequency-matched decay LW's [Eq. (34)], and the hyperbola represents the locations in k space where the TPD growth rate is maximized [Eq. (35)]. The intersections of the circle and the hyperbolae are the spectral locations where TPD LW's are expected to occur. Labels 1 and 2 denote the forward propagating (blue-shifted) and backward propagating (red-shifted) LW's, respectively.

correspond to forward-propagating, blue-shifted LW's and the two modes labeled "2" at $\mathbf{k}\lambda_{\text{De}} = (-0.038, \pm0.087)$ correspond to backward-propagating, red-shifted plasmons.

Figure 122.27 shows the normalized LW spectra

$$W_k \equiv \frac{x_{\max}}{2\pi}\frac{y_{\max}}{2\pi}\frac{\left|E_{\text{LW}}\left(k_x,k_y\right)\right|^2}{4\pi n_{\text{e0}}T_{\text{e0}}},$$

time-averaged over the full 20-ps duration of the simulation, for both the (a) RPIC and (b) ZAK models. The RPIC and ZAK results are displayed on the same color scale to facilitate a direct comparison. The RPIC and ZAK results exhibit good qualitative similarity, with the dominant spectral features falling at exactly the same location in k space. The labels 1 and 2 in Fig. 122.27 refer to the same unstable modes as were identified previously in Fig. 122.26. In addition, two LDI steps of the blue-shifted plasmons are seen in the RPIC calculations [labeled 1′ and 1″, respectively, in Fig. 122.27(a)], while only one LDI step is clearly seen in the ZAK calculations [labeled 1′ in Fig. 122.27(b)]. As a measure of the level of laser-induced LW excitation, the integrated value $\mathcal{W} \equiv \int \mathrm{d}\mathbf{k}W_k$ is defined, where the integration is carried out over the disk $|\mathbf{k}\lambda_{\mathrm{De}}| \leq 0.25$. For the RPIC simulation $\mathcal{W} = 1.0 \times 10^{-1}$, while the ZAK simulation gives the almost 2× stronger value of $\mathcal{W} = 1.8 \times 10^{-1}$. However, the peak values in the RPIC simulation are narrower and more intense than for the ZAK case.

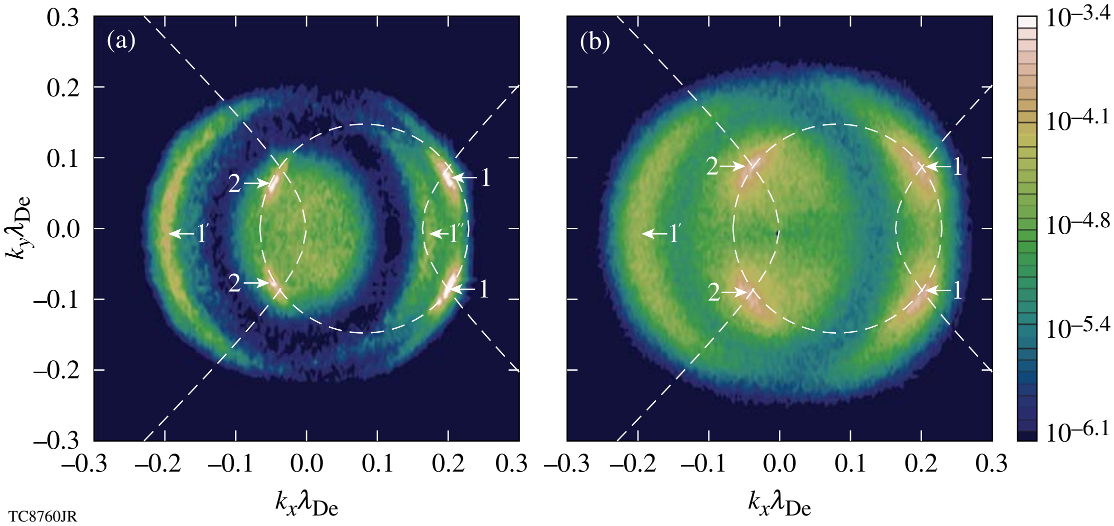

Figure 122.27
The time-averaged LW spectral intensity W_k is shown for both (a) RPIC and (b) ZAK simulations for a single plane-wave pump light wave and the parameters $T_{e0} = 4$ keV and $n_{e0}/n_c = 0.23$. Labels 1 and 2 denote the forward-propagating (blue-shifted) and backward-propagating (red-shifted) TPD LW's, respectively. Label 1′ indicates that the LW's wave corresponding to the first LDI step of blue TPD plasmon (1), which is evident in both the RPIC and ZAK calculations. The second decay step (1″) can be seen in (a).

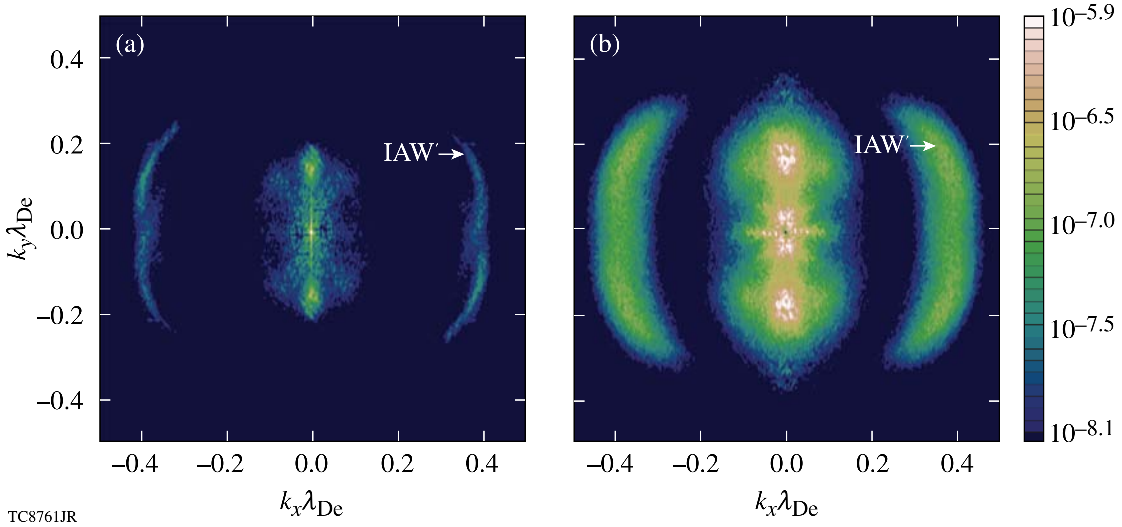

Figure 122.28
The time-averaged IAW density fluctuation spectrum $|\delta N_k|^2$ is shown for (a) RPIC and (b) ZAK simulations of TPD driven by a single plane-wave pump with the parameters $T_{e0} = 4$ keV and $n_{e0}/n_c = 0.23$. IAW's corresponding to the first LDI step of the blue TPD plasmon are evident in both sets of simulations, although narrower and weaker in (a) than in (b), and are indicated by the label IAW′.

The corresponding IAW spectra

$$\left|\delta N_k\right|^2 \equiv \frac{x_{\max}}{2\pi}\,\frac{y_{\max}}{2\pi}\left|\delta n_{eS}\left(k_x,k_y\right)\Big/n_{e0}\right|^2$$

are shown in Fig. 122.28. Ion-acoustic waves caused by LDI are clearly visible in both the RPIC and ZAK simulations and are labeled IAW′. The IAW from the second LDI step is very weak and difficult to identify in the displayed spectrum. The integrated LDI density perturbations are estimated by the quantity $\mathcal{N}_{\text{LDI}} \equiv \int \mathrm{d}\mathbf{k}\left|\delta N_k\right|^2$. In this case, the domain of integration is the annulus $0.3 \le \left|\mathbf{k}\lambda_{\text{De}}\right| \le 0.5$. The choice of domain is intended to avoid including the structures in $\left|\delta N_k\right|^2$ found near $k_x = 0$ that arise from the beating of pairs of LW's with equal and opposite values of k_y and equal values of k_x. Using this criterion, RPIC gives $\mathcal{N}_{\text{LDI}} = 1.4 \times 10^{-4}$, whereas ZAK gives $\mathcal{N}_{\text{LDI}} = 5.3 \times 10^{-4}$. If it is assumed that the ponderomotive drive for the IAW's is proportional to $\mathcal{W}$, comparing the $\mathcal{N}_{\text{LDI}}$ values would indicate that LDI plays a relatively smaller role in the nonlinear saturation in RPIC. Kinetic saturation mechanisms, such as trapping of electrons (and ions) in the LW's (and IAW's) in the case of RPIC, cannot be ruled out. All of the simulations reported here reach saturation after about 15 ps, which is also the time at which LDI features become well established in the spectra.

In the second simulation set, two overlapping incident laser beams, again plane waves, were prescribed at angles θ relative to the x axis of $\theta_{\pm} = \pm 23°$. This type of crossed-beam geometry is generic to direct-drive ICF, where large numbers of beams are overlapped to provide uniform illumination of the target (the precise angles of $\theta_{\pm} = \pm 23°$ are specific to OMEGA[1]). The individual beam intensity $I_0 = 1 \times 10^{15}$ W/cm^2 was chosen such that the crossed-beam overlapped intensity was the same as the previous single-beam case, shown in Figs. 122.26–122.28, and all other parameters were identical, with the exception of the plasma density, which was slightly increased to $n_{e0}/n_c = 0.231$ (the reason for choosing this particular density is given below).

The locations of the most linearly unstable TPD-produced LW waves, for an arbitrary irradiation angle in a homogeneous plasma, can be obtained simply by rotating Eqs. (34) and (35) in k space (see **Appendix C**, p. 109). In general, for two overlapping beams there are eight distinct LW's since each beam will produce four LW's (as previously shown in Fig. 122.26): two corresponding to the forward (blue-shifted) plasmons and two corresponding to the backward (red-shifted) plasmons. In the case of beams symmetrically oriented about the x axis, for a given set of plasma parameters $\left(T_{e0} \text{ and } 0.2 \lesssim n_{e0}/n_c \lesssim 0.25\right)$, a particular beam angle θ exists in which two of the forward (blue-shifted) plasmons are degenerate, or common. This overlap, or sharing of a common plasmon, allows for the cooperative nonlinear interaction between the two crossed beams. Conversely, for a prescribed beam angle θ and electron temperature T_{e0}, a particular density n_{e0}/n_c exists that will result in degenerate forward plasmons. In monotonic inhomogeneous plasmas, a location will always exist along the beam path where this degeneracy condition is satisfied, but in homogeneous simulations it must be specially selected, which is the choice made here. The relationship between the beam angle θ, electron density n_{e0}/n_c, and electron temperature T_{e0} for degeneracy to occur is derived in **Appendix C** and is given by Eq. (C8). For an electron temperature $T_{e0} = 4$ keV and angles $\theta_{\pm} = \pm 23°$, Eq. (C8) yields degenerate forward plasmons for an electron density of $n_{e0}/n_c = 0.231$. This is depicted graphically in Fig. 122.29, where two sets of circles and hyperbolae are shown: (1) solid lines for the laser propagating at $\theta_{+}(= +23°)$ and (2) dashed lines for the laser propagating at $\theta_{-}(= -23°)$. As before, the intersections of the circle and the hyperbola for

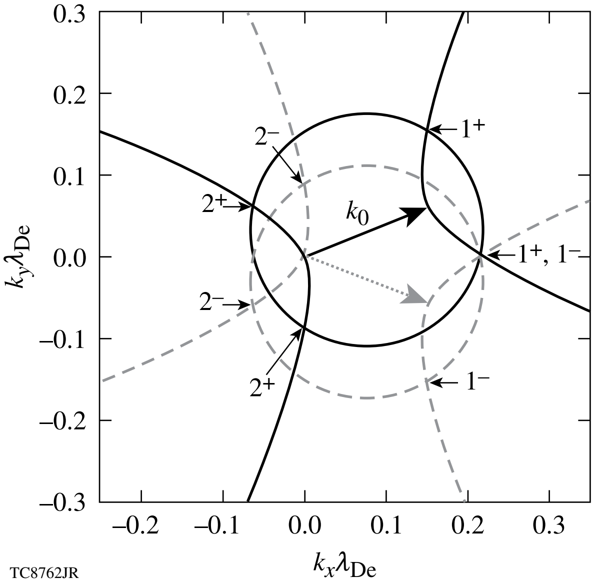

Figure 122.29
Expected wave numbers for TPD LW's resulting from the decay of two EM plane waves propagating with angles $\theta = \pm 23°$ with respect to the x axis (the parameters are $T_e = 4$ keV and $n_e/n_c = 0.231$). Points 1^+ (1^-) and 2^+ (2^-) denote the expected locations of the red- and blue-shifted plasmons from the EM wave propagating with angle $\theta = +23°$ ($-23°$), respectively. The solid (dashed) circle [Eq. (C1)] represents all frequency- and wave-number–matched LW's for the $\theta = +23°$ ($-23°$) beam. Likewise, the solid (dashed) hyperbolae [Eq. (C4)] show the maximum growth rate for the $\theta = +23°$ ($-23°$) beam. The blue-shifted plasmons 1^+ and 1^- are degenerate.

each respective laser beam are the spectral locations where LW's are expected to be observed. These are labeled as in Fig. 122.26, with the superscripts ± corresponding to decays of the beam incident at angle $\theta_{\pm}$. The on-axis, blue-shifted LW's of both beams (1^+ and 1^-) are degenerate—the common LW wave. This has a wave number $\mathbf{k}\lambda_{\mathrm{De}} \approx (0.23,0.0)$ and a phase velocity $v_\phi / v_{\mathrm{the}} \approx 4.7$. This notion of a "shared" plasma wave, which can generally occur in cases of multiple-beam irradiation where a symmetry exists, has been discussed by Short *et al.*[21]

Figures 122.30 and 122.31 show the LW spectral intensity W_k and IAW density spectra $|\delta N_k|^2$, respectively, time averaged over the full 20-ps duration of the simulation. Although the RPIC and ZAK results are not in exact quantitative agreement,

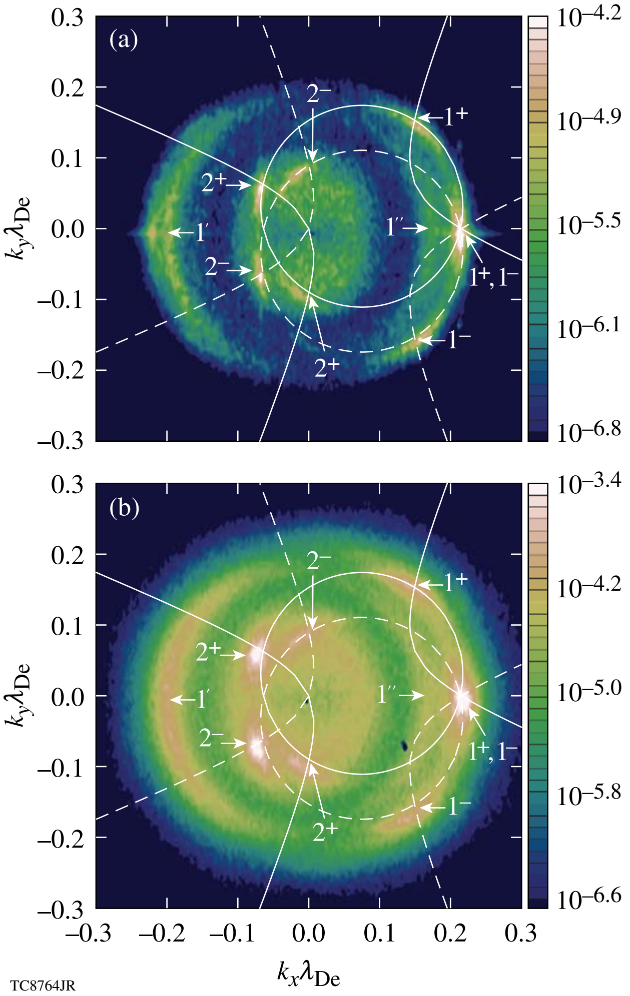

Figure 122.30
The time-averaged LW spectrum W_k is shown for both (a) RPIC and (b) ZAK simulations for the parameters T_{e} = 4 keV and $n_{\mathrm{e}}/n_{\mathrm{c}} = 0.231$. The pump consists of two identical EM plane waves, of intensity $I_0 = 1 \times 10^{15}$ W/cm^2, propagating obliquely at $\theta = \pm 23°$ with respect to the x axis. Locations 1^+ (1^-) and 2^+ (2^-) denote the blue- and red-shifted LW's produced by the pump laser with angle $\theta = +23°$ (–23°), respectively. The forward-going, blue-shifted LW's from each beam that are on-axis ($k_y = 0$) are degenerate. The waves marked 1′ and 1″ are identified as the LW's produced by the first and second LDI steps of the degenerate LW, respectively.

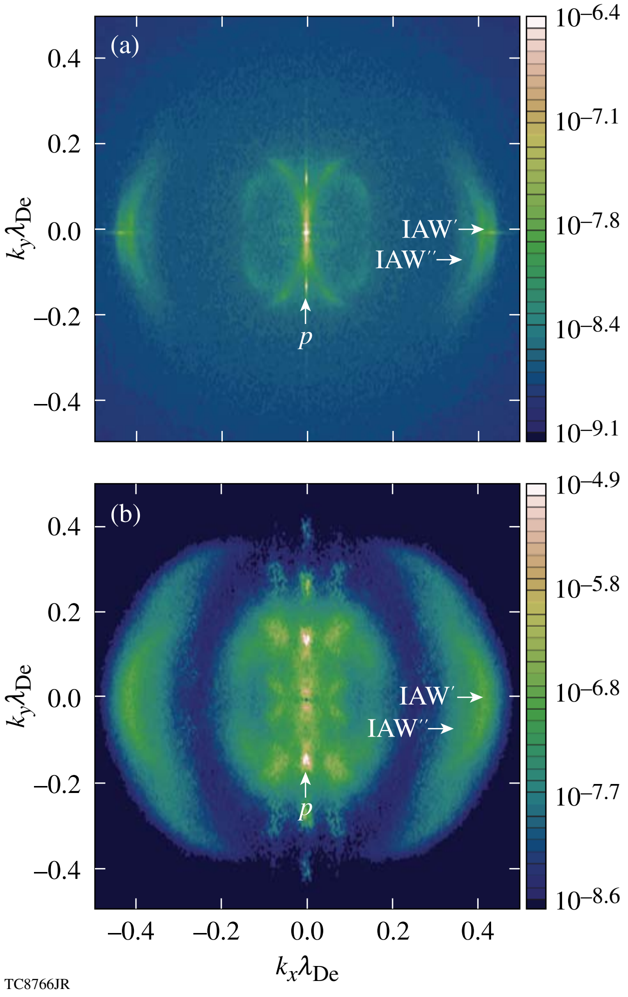

Figure 122.31
The time-averaged IAW spectrum $|\delta N_k|^2$ is shown for (a) RPIC and (b) ZAK simulations with the parameters T_{e} = 4 keV and $n_{\mathrm{e}}/n_{\mathrm{c}} = 0.231$. The pump consists of two EM plane waves, of intensity $I_0 = 1 \times 10^{15}$ W/cm^2, propagating obliquely with angle $\theta = \pm 23°$ with respect to the x axis. The features labeled IAW′ and IAW″ are IAW's generated by the first and second decay steps of the LDI of the common (degenerate) TPD LW. The feature indicated by the label p, with $k_x\lambda_{\mathrm{De}} = 0$, is the density response to the ponderomotive force generated by the beating of the two incident plane waves at $k_y\lambda_{\mathrm{De}} = \pm 2k_0\lambda_{\mathrm{De}} \sin(23°) \sim \pm 0.123$.

their fluctuation spectra have strikingly similar features. The dominant spectral features occur at precisely the same locations in k space. In Figs. 122.30(a) and 122.30(b), all eight of the single-beam decays ($1^{\pm}$, $2^{\pm}$) can be seen, with the strongest spectral feature that of the degenerate, blue-shifted LW (1^{+},1^{-}). In addition, two LDI decay steps of the forward-TPD–produced LW's can be seen in both the RPIC and the ZAK calculations [indicated by the labels $1'$ at $\mathbf{k}_{1'}\lambda_{\text{De}} \approx (-0.20,0.0)$ and $1''$ at $\mathbf{k}_{1''}\lambda_{\text{De}} \approx (0.16,0.0)$ (Ref. 22)]. For the RPIC simulation, the LW excitation was computed to be $\mathcal{W} = 2.7 \times 10^{-2}$, while the ZAK simulation has a significantly stronger level of LW's, $\mathcal{W} = 2.8 \times 10^{-1}$. Figure 122.31 shows the IAW's associated with these two LDI decay steps, $\mathbf{k}_{\text{IAW}'}\lambda_{\text{De}} \approx (0.43,0)$ and $\mathbf{k}_{\text{IAW}''}\lambda_{\text{De}} \approx (0.39,0)$ (Ref. 22), although the IAW from the second decay is relatively weak and not distinctly evident in the ZAK calculations [Fig. 122. 31(b)]. As a measure of the strength of the LDI process, RPIC gives $\mathcal{N}_{\text{LDI}} = 6.4 \times 10^{-5}$, whereas ZAK gives $\mathcal{N}_{\text{LDI}} = 3.7 \times 10^{-4}$. Again these comparisons of the $\mathcal{N}_{\text{LDI}}$ values would indicate that LDI plays a relatively smaller role in the nonlinear saturation in RPIC compared to its role in ZAK. Another feature (p) evident in Fig. 122.31, although unrelated to LDI, are fluctuations at $\mathbf{k}\lambda_{\text{De}} \approx (0.0, \pm 0.123)$ caused by the ponderomotive force that results from the beating of the two incident light waves in the transverse direction at $k_y\lambda_{\text{De}} = \pm 2k_0\lambda_{\text{De}} \sin(23°)$. Other features near $k_x = 0$ are caused by the beating of LW's with equal values of k_x and equal and opposite values of k_y.

The electron distribution computed from discrete simulation particles provides information regarding suprathermal electron generation. The energetic electron tails are often noisy, however, because of insufficient particle numbers. To improve the statistics, the electron distribution was time averaged over 20 ps. To provide information regarding the directionality of energetic electron generation, the (time-averaged) 2-D electron distribution function $f(v_x,v_y)$ was collapsed to 1-D as follows: First, the 2-D distribution f' was computed in a rotated (primed) velocity frame, where the v'_x direction is parallel to the desired probe angle θ_{probe}:

$$f'\left(v'_x,v'_y\right) = f\left(v'_x\cos\theta_{\text{probe}} + v'_y\sin\theta_{\text{probe}}\right.$$

$$\left. - v'_x\sin\theta_{\text{probe}} + v'_y\cos\theta_{\text{probe}}\right).$$

The distribution f' was then integrated in the perpendicular v'_y direction, within the limits $\pm 2v_{\text{the}}$, to yield a 1-D velocity distribution,

$$f_{\text{1-D}}\left(v'_x\right) \equiv \int_{-2v_{\text{the}}}^{2v_{\text{the}}} f'\left(v'_x,v'_y\right)dv'_y .$$

Typically, the angle θ_{probe} is chosen so that the v'_x axis aligns with the direction of the LW propagation. With this choice of θ_{probe},$f_{\text{1-D}}(v'_x)$ yields a 1-D velocity distribution, and therefore a hot electron temperature, in the direction of LW propagation.

The time-averaged 1-D electron-distribution function $f_{\text{1-D}}$ along the common wave direction [$\theta_{\text{probe}} = 0$, shown in Fig. 122. 32(a)] indicates a hot-electron temperature of approximately 3× the initial background electron temperature $T_{\text{hot}} \sim 3T_{\text{e0}}$, where $T_{\text{e0}} = 4$ keV. Although the electrons have departed from their initial Maxwellian state, the hot-electron temperature is modest. Since our electron distribution was averaged over 20 ps and the simulation required 15 ps to reach saturation, it is possible that if the simulation were continued longer in time, the electron distribution would continue to evolve toward higher hot-electron temperatures. An often-used simple estimate of hot-electron temperature, based on a single-plane LW, is $T\big/T_{\text{e0}} \sim \left(v_{\phi}\big/v_{\text{the}}\right)^2 = 22$ (Ref. 23). This estimate is in excess of our observed hot-electron temperature by a factor of about 7.4, although $v_{\phi}^2\big/v_{\text{the}}^2 = 22$ is exactly the place where the distribution function begins to deviate from a Maxwellian [indicated by the arrows in Fig. 122. 32]. The probe direction $\theta_{\text{probe}} = 180°$ [see Fig. 122. 32(b)] gives a measure of hot-electron generation by the LDI-produced LW, with $T_{\text{hot}}\big/T_{\text{e0}} \sim 3$. Hot-electron temperatures along the other principal directions of $\theta_{\text{probe}} = \pm 23°$ (directions of the non-degenerate forward blue-shifted plasmons; results not shown) also indicate $T_{\text{hot}}\big/T_{\text{e0}} \sim 3$. In this particular case, the hot-electron temperature does not appear to be significantly directional.

One observation to be drawn from the single-beam and overlapping-beam simulations shown above is that while the single-beam and the overlapped intensities are identical ($\Sigma I_0 = 2 \times 10^{15}$ W/cm^2), the peak value of the LW spectrum for the overlapping-beams case (Fig. 122.30) is greater than that for the single-beam case (Fig. 122.27), while for the RPIC runs, the integrated spectrum is actually weaker: $\mathcal{W} = 1.0 \times 10^{-1}$ for the single-beam case (Figs. 122.26–122.28) while $\mathcal{W} = 2.7 \times 10^{-2}$ for the overlapping-beam case (Figs. 122.29–122.32). This is understandable if one considers the single-beam case with $I_0 = 2 \times 10^{15}$ W/cm^2 (Figs. 122.26–122.28) as two perfectly coincident beams, each with an intensity of 1×10^{15} W/cm^2. Consequently, each one of the four TPD-produced LW's has a corresponding overlapped LW. In the case of two beams propagating at angles $\theta = \pm 23°$ (Figs. 122.29–122.32), only one

TPD-produced LW has a corresponding overlapped LW (location $1^{\pm}$ shown in Fig. 122.29). The fact that the peak intensity is higher is evidence that overlapping LW's enhance the TPD instability by allowing for nonlinear interaction between the crossing laser beams.

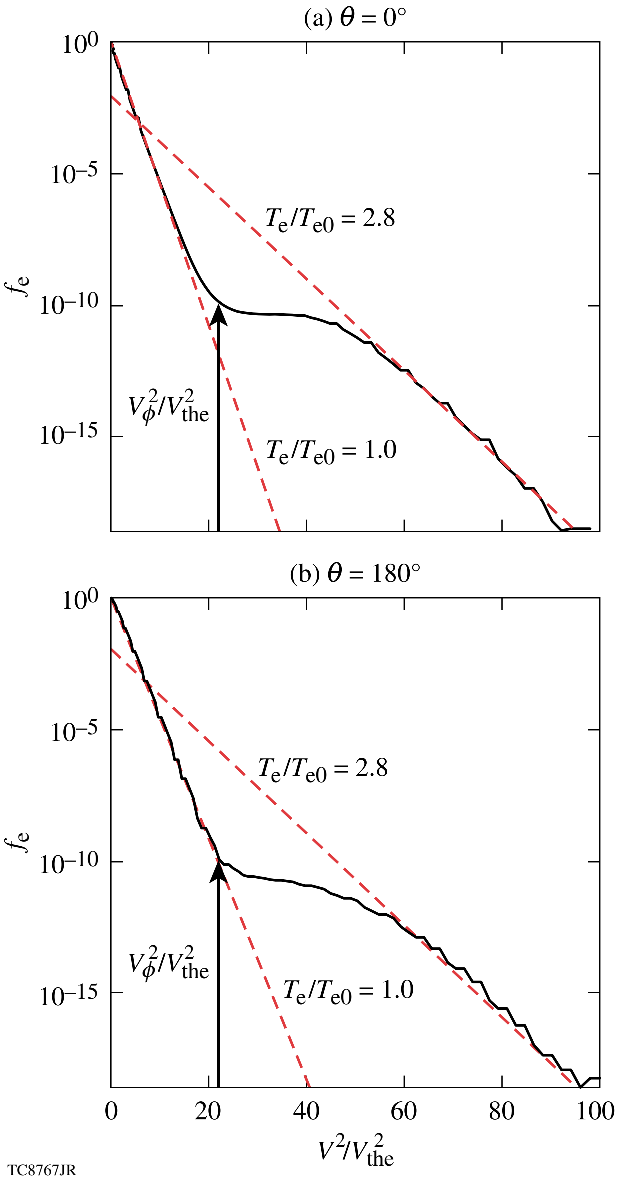

Figure 122.32
The 1-D time-averaged electron distribution shown along two directions ($\theta = 0°, 180°$) for two obliquely incident EM plane waves (at angles ±23° with respect to the x axis) with individual intensities of $I_0 = 1 \times 10^{15}$ W/cm^2 and parameters $T_{e0} = 4$ keV, $n_{e0}/n_c = 0.231$. The angle $\theta = 0°$ (a) corresponds to the direction of the common LW, while the angle $\theta = 180°$ (b) corresponds to the LDI LW direction of the common wave. The arrows indicate the value of v^2/v_{the}^2 corresponding to the phase velocity of the common wave.

In the final simulation set, the electron temperature was reduced to $T_{e0} = 2$ keV, which is typical of current OMEGA implosion experiments.[1] For this electron temperature and beam angle $\theta_{\pm} = \pm 23°$, Eq. (C8) gives an electron density $n_{e0}/n_c = 0.241$, at which the simulations were performed. This was done to involve the shared plasma wave since it is believed to be important experimentally.[1] The laser geometry and intensity ($I_0 = 1 \times 10^{15}$ W/cm^2 for each beam) are identical to those corresponding to the previous case in Figs. 122.29–122.32. The individual beam intensity of 1×10^{15} W/cm^2 corresponds to a linear (amplitude) growth rate $\gamma_{TPD}/\omega_{pe0} \simeq 4.3 \times 10^{-3}$, which is 83× above the single-beam collisional threshold (the collisional frequency ν_{e0}/ω_{pe0} is taken to be $\sim 4.7 \times 10^{-4}$). This final case is therefore more strongly driven than the second case, which was 50× the collisional threshold. The linear TPD wave geometry is illustrated in Fig. 122.33, the labels having the same meaning as in previous figures. The common LW now occurs at $\mathbf{k}\lambda_{De} \approx (0.16, 0.0)$ and corresponds to a phase velocity $v_\phi/v_{the} \approx 6.5$.

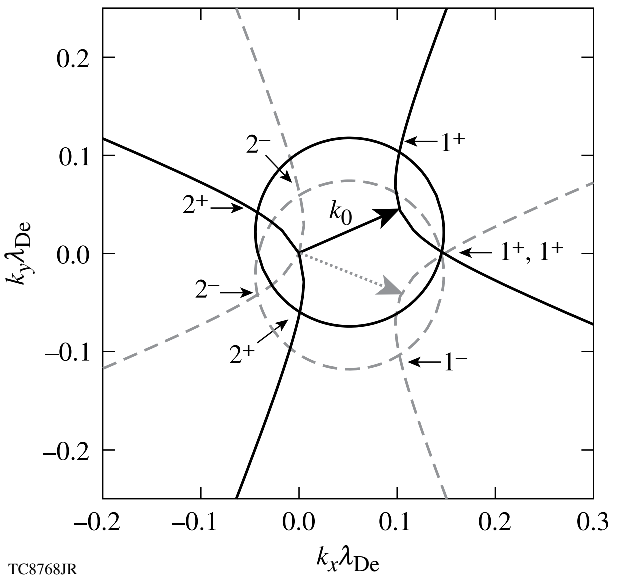

Figure 122.33
Decay diagram for the TPD instability of two EM plane-wave pump beams propagating with angles $\theta = \pm 23°$ relative to the x direction in a plasma with $T_e = 2$ keV and $n_e/n_c = 0.241$. The solid (dashed) curves correspond to the individual decays of the beam with incident angle of $\theta = +23°$ (–23°). The intersections of the circles (which specify frequency and wave-number matching) and the hyperbolae (which are the locations of maximum growth rate) [Eqs. (C1)–(C4)] that are labeled 1 and 2 give the expected location of the blue- and red-shifted TPD LW's, respectively. The on-axis ($k_y\lambda_{De} = 0$) blue-shifted LW's are degenerate.

Figures 122.34 and 122.35 show the normalized LW spectral intensity W_k and the IAW density spectra $|\delta N_k|^2$, respectively, time averaged over 20 ps. The RPIC and ZAK results bear similar qualitative behavior to the $T_e = 4$ keV case when the reduction of $k\lambda_{De}$ is taken into account. Both the LW and IAW spectral features in the RPIC simulations are significantly nar-

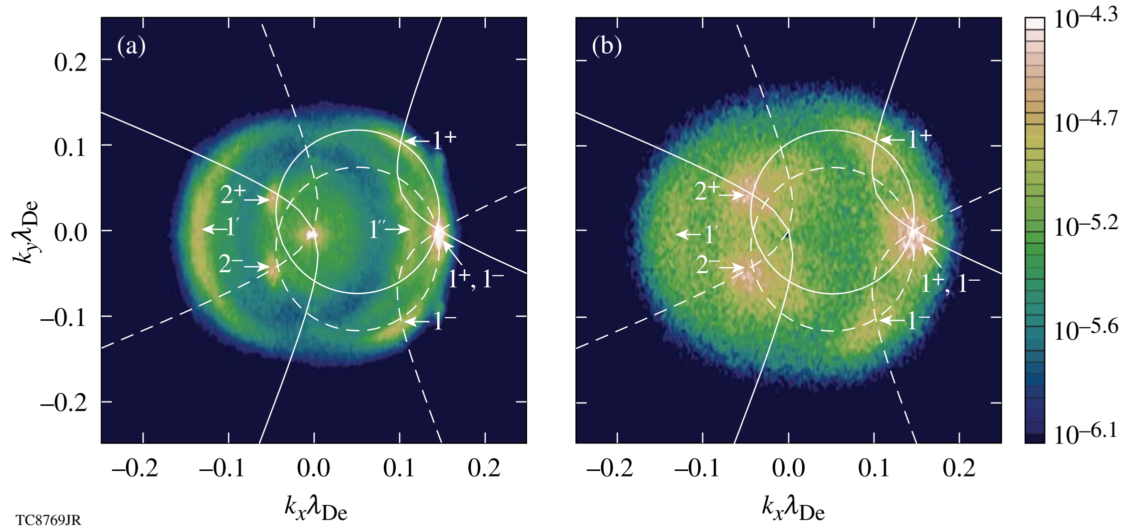

Figure 122.34
The time-averaged LW spectrum W_k is shown for (a) RPIC and (b) ZAK simulations for the parameters $T_e = 2$ keV and $n_e/n_c = 0.241$. The pump consists of two plane EM waves propagating at angles $\theta = \pm 23°$ with respect to the x axis. Each pump laser beam has an intensity of $I_0 = 1 \times 10^{15}$ W/cm^2. The labels 1^+ (1^-) identify the forward-propagating, blue-shifted LW's resulting from the primary decay of the beam with angle $\theta = +23°$ (–23°), while the labels 2^+ (2^-) mark the corresponding backward-propagating, red-shifted LW's. The degenerate LW is seen to dominate both the (a) RPIC and (b) ZAK spectra. The features marked $1'$ and $1''$ are identified as the first and second decay steps of the LDI of the shared LW. The second step is not seen in the ZAK calculations (b).

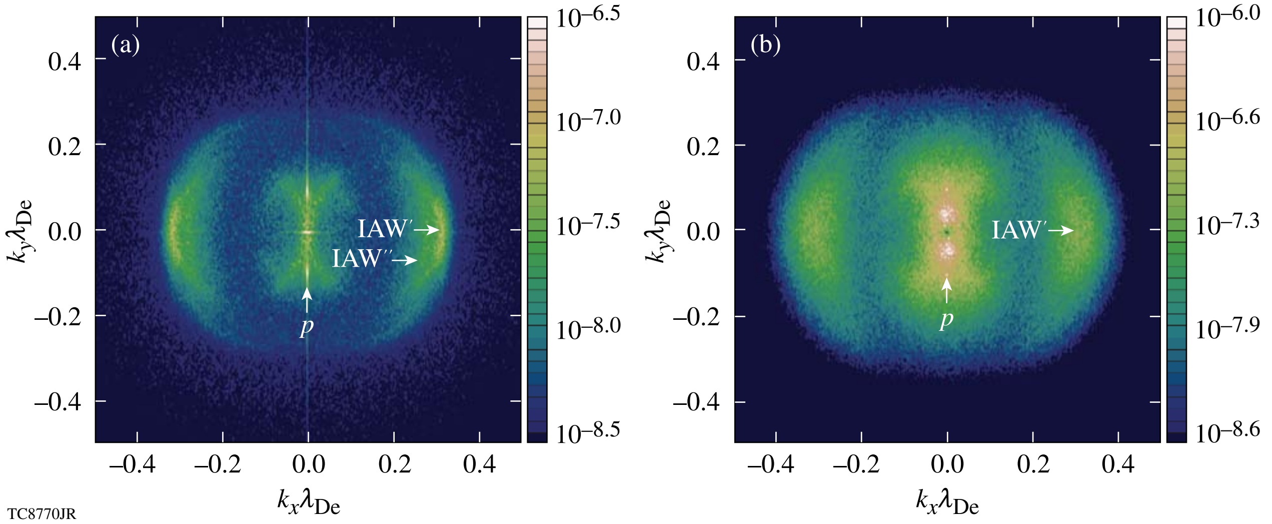

Figure 122.35
The time-averaged IAW spectrum $|\delta N_k|^2$ is shown for (a) RPIC and (b) ZAK simulations for the case with parameters $T_e = 2$ keV and $n_e/n_c = 0.241$. The pump consists of two plane EM waves propagating with angles $\theta = \pm 23°$ with respect to the x axis, each with an intensity of $I_0 = 1 \times 10^{15}$ W/cm^2. The features labeled IAW′ and IAW″ are IAW's generated by the first and second decay steps of the LDI of the common (degenerate) TPD LW. The second step is seen only in the RPIC calculation (a). The feature indicated by the label p, with $k_x\lambda_{De} = 0$, is the density response to the ponderomotive force generated by the beating of the two incident plane waves at $k_y\lambda_{De} = \pm 2k_0\lambda_{De}\sin(23°) \sim \pm 0.09$.

rower and weaker than those of the ZAK simulations (RPIC: $\mathcal{W} = 4.5 \times 10^{-2}$, ZAK: $\mathcal{W} = 8.6 \times 10^{-2}$; for the LDI process, RPIC: $\mathcal{N} = 1.9 \times 10^{-4}$, ZAK: $\mathcal{N}_{\mathrm{LDI}} = 4.3 \times 10^{-4}$). The RPIC LW spectrum [Fig. 122.34(a)] contains evidence of two LDI decay steps of the common LW: the primary LDI step, marked with the label 1′, at $\mathbf{k}_{1'}\lambda_{\mathrm{De}} \approx (-0.13,0.0)$ and a second LDI step, marked 1″ at $\mathbf{k}_{1''}\lambda_{\mathrm{De}} \approx (0.09,0.0)$ (Ref. 22). The RPIC IAW spectrum [Fig. 122.35(a)] also shows the IAW's corresponding to these two LDI decay steps [$\mathbf{k}_{\mathrm{IAW}'}\lambda_{\mathrm{De}} \approx (0.29,0.0)$ and [$\mathbf{k}_{\mathrm{IAW}''}\lambda_{\mathrm{De}} \approx (0.25,0.0)$ (Ref. 22)], although the IAW from the second decay is relatively weak. Only one LDI step is clearly evident in the ZAK calculations [Figs. 122.34(b) and 122.35(b)]. The distinctive fluctuations in the IAW spectrum $|\delta N_k|^2$ at $\mathbf{k}\lambda_{\mathrm{De}} \approx (0.0, \pm 0.09)$ are again due to ponderomotive force generated by the beating of the two obliquely propagating incident light waves. Although not shown, the difference between the two calculations can be reduced by comparing the ZAK spectra with those of RPIC carried out at a higher intensity. Results (not shown) indicate that the LW and IAW spectra in RPIC simulations broaden significantly. This observation is consistent with past experience.[11,24]

The time-averaged (over 20 ps), 1-D electron-distribution function along the common-wave direction ($\theta_{\mathrm{probe}} = 0$), shown in Fig. 122.36(a), gives $T_{\mathrm{hot}}/T_{\mathrm{e0}} \sim 14$. Again, the simple estimate of hot-electron temperature is $T_{\mathrm{hot}}\big/T_{\mathrm{e0}} \sim \left(v_\phi/v_{\mathrm{the}}\right)^2 = 42$ (Ref. 23). This estimate is in excess of the observed hot-electron temperature by a factor of ~3. The simple estimate $T_{\mathrm{hot}}\big/T_{\mathrm{e0}} = \left(v_\phi/v_{\mathrm{the}}\right)^2$, based on a single-plane LW, is not accurate here because the LW spectrum contains a broad and complex spectrum of waves. The phase velocity of the common wave is, however, close to the position where the distribution function first begins to deviate from the initial Maxwellian (shown by the arrows in Fig. 122.36). The hot-electron temperature in the LDI direction of the common LW wave ($\theta_{\mathrm{probe}} = 180°$), shown in Fig. 122.36(b), is cooler with $T_{\mathrm{hot}}/T_{\mathrm{e0}} \sim 10$ most likely because the LDI-produced LW's are not as strong as the primary LW. The phase velocities of the primary and LDI LW's differ only slightly. The hot-electron temperatures along the other principal directions $\theta_{\mathrm{probe}} = \pm 23°$ (results not shown) were also determined to be $T_{\mathrm{hot}}/T_{\mathrm{e0}} \sim 10$. The hot-electron temperatures for the $T_{\mathrm{e0}} = 2$ keV case are significantly higher than that for the $T_{\mathrm{e0}} = 4$ keV case. The intensities of the degenerate LW's for the two temperature cases do not differ significantly. The TPD-produced LW's for an electron temperature of $T_{\mathrm{e0}} = 2$ keV occur at lower values of $k\lambda_{\mathrm{De}}$ and therefore have greater phase velocities since

$$v_\phi/v_{\mathrm{the}} = \left[1 + (3/2)(k\lambda_{\mathrm{De}})^2\right]\Big/(k\lambda_{\mathrm{De}}).$$

Waves with greater phase velocity may lead to higher hot-electron temperatures, even though T_{hot} is not seen to scale as strongly as $\left(v_\phi/v_{\mathrm{the}}\right)^2$, as might be suggested by the simple, single-plane-LW estimate.

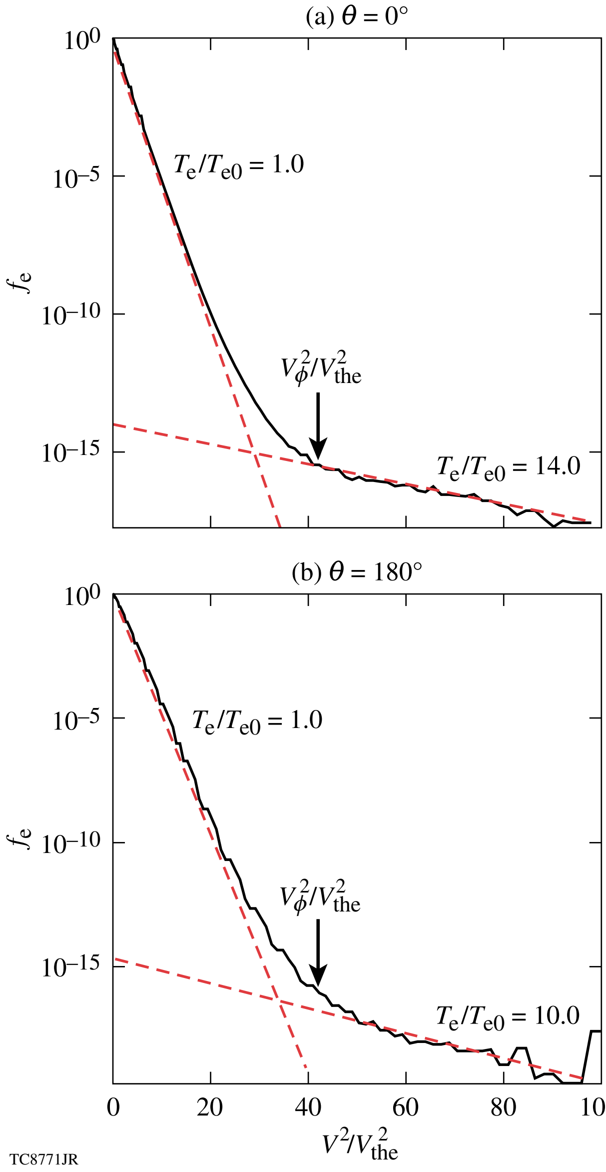

Figure 122.36
The 1-D, time-averaged electron distribution shown along two directions [$\theta = 0°$ (top panel) and $\theta = 180°$ (bottom panel)] for the case of two EM plane waves, each of intensity $I_0 = 1 \times 10^{15}$ W/cm^2, that are incident at angles of $\theta = \pm 23°$ on a plasma with $T_e = 2$ keV and $n_e/n_c = 0.241$. The temperature in the direction $\theta = 0\left(T_{\mathrm{hot}}/T_{\mathrm{e0}} = 14\right)$, as determined by the fit shown by the red dashed curves, is greater than that in the direction $\theta = 180°\left(T_{\mathrm{hot}}/T_{\mathrm{e0}} = 10\right)$. The arrows indicate the value of v^2/v_{the}^2 corresponding to the phase velocity of the common LW.

Summary and Conclusions

The purpose of this article has been to present the RPIC model for TPD and to establish it as a useful and reliable model for simulating the nonlinear development of TPD. The simulations were performed in homogeneous plasmas to facilitate comparisons with linear theory. Given the encouraging results in homogeneous plasma, the next step in the development of the RPIC TPD model will be to introduce experimentally relevant density gradients and flow velocities.

The RPIC model and the Zakharov limit were compared for three separate cases. In all three cases, shown in **Simulation Results** (p. 92), the level of LW turbulence excited by TPD was lower in RPIC than in ZAK, although both models displayed qualitatively similar *k*-space fluctuation spectra. Therefore, kinetic effects—primarily hot-electron generation—are likely a competing saturation mechanism together with LDI. This is consistent with the results of several previous works.[11,24] Further research is required to determine the relative importance of LDI and hot-electron generation when they act simultaneously.

Two of the three cases investigated TPD excited by crossing laser beams. These simulations show that at a certain density, for a given angle between the beams, the beams can share a common primary LW, thereby enhancing the TPD instability (in an inhomogeneous plasma such a density can always be found, but here it was chosen by design). The saturation of the crossed-beam TPD instability by LDI and modification of the electron-distribution function is also apparent. The heated-electron–distribution function was observed to deviate from the initial Maxwellian at a velocity corresponding to the phase velocity of the common LW. Crossed-beam irradiation also introduced a nonzero ponderomotive force in the electron equation of motion from the transverse electric field. The effects of this term were observed in the perturbed density spectra. A strong feature in the low-frequency density fluctuation spectrum also resulted from the ponderomotive beating of two LW's sharing the same parallel wave number (with respect to the laser direction) but with equal and opposite perpendicular wave numbers.[14] This feature was also evident in our previous ZAK simulations but never noted, which would imply that density channels are produced parallel to the laser direction. Whether this survives in an inhomogeneous plasma remains to be studied.

The semi-quantitative agreement of RPIC modeling and ZAK modeling, for the few survey cases presented here, highlights the similarities and differences between the kinetic RPIC model and its limiting (fluid) form. In this way, the RPIC modeling provides a bridge to systematically improve upon ZAK modeling. This is desirable because fluid-type codes are much more efficient than PIC codes and can therefore include more of the essential experimental realities (e.g., three spatial dimensions and speckled laser beams). Of particular interest is the possibility, currently under investigation, that the discrepancy between the two models might be recoverable by including modifications of the electron-distribution function in the quasi-linear approximation.[11] If possible, this would have the benefit of greatly reduced computational expense, allowing for more-realistic simulations to be made, for example, in three spatial dimensions. The resulting modified electron energy distributions are expected to be strongly dependent on the boundary conditions used for electrons entering and leaving the simulation box (this is consistent with conclusions in Sanbonmatsu *et al.*[11]). Indeed, the present calculations should not be regarded as predicting experimental hot-electron spectra since it has been argued that the recirculation of hot electrons through the TPD-active region must be accounted for by any physically realistic model of hot-electron generation in spherical implosions.[20]

Finally, the currents generating experimentally observable EM signatures of TPD (the secondary radiation emissions at $\omega_0/2$ and $3\omega_0/2$), which typically involve a tiny fraction of the LW and IAW energy, can be calculated by postprocessing the high-frequency electric-field envelopes and the low-frequency electron-density fluctuations generated in either the RPIC or the ZAK modeling. This technique is exactly the same as used in Refs. 9 and 17 for the ZAK modeling. This is another advantage of the RPIC modeling, which uses the same envelope representations as ZAK, over standard PIC methods. With this procedure future studies of the correlation of hot-electron effects with $\omega_0/2$ radiation may be possible.

ACKNOWLEDGMENT

We are pleased to acknowledge useful discussions with Drs. A. V. Maximov, W. Seka, R. W. Short, and B. Langdon.

This research was supported by (1) the U.S. Department of Energy, Office of Inertial Confinement Fusion under Cooperative Agreement No. DE-FC52-08NA28302, the University of Rochester, and the New York State Energy Research and Development Authority and (2) the National Nuclear Security Agency through its High-Energy-Density Laboratory Plasmas Grant No. DE-FG52-09NA29545. The support of DOE does not constitute an endorsement by DOE of the views expressed in this article.

Appendix A: Derivation of the RPIC Equations

In this Appendix, a derivation of the RPIC model is presented. One notable difference between standard PIC methods and RPIC is the explicit removal of the laser time scale from

RPIC equations of motion. As a result of removing the laser time scale, it is essential that RPIC equations of motion are expressed in an oscillating, non-inertial frame. There are three major components of the RPIC derivation: the electron equation of state (closure for our RPIC model), the nonlinear Schrödinger equation (EM propagation and pump depletion model), and the reduced-description particle equations of motion.

1. Electron Equation of State

Assume that the velocity $\tilde{\mathbf{U}}$, electrostatic potential ϕ, and pressure p are of the following form:

$$\tilde{\mathbf{U}} = \tilde{\mathbf{U}}_S + \frac{1}{2}\left[\tilde{\mathbf{U}}_F \exp\left(-i\omega_{\mathrm{LW}}t\right) + \mathrm{c.c.}\right].$$

$$\phi = \phi_S + \frac{1}{2}\left[\phi_F \exp\left(-i\omega_{\mathrm{LW}}t\right) + \mathrm{c.c.}\right],$$

$$p \approx p_S.$$

Substituting the above expression for $\tilde{\mathbf{U}}$ into Eq. (18), keeping only terms of frequencies $\omega = 0$, $\pm\omega_{\mathrm{LW}}$, $\pm(\omega_0-\omega_{\mathrm{LW}})$, $\pm(\omega_0-2\omega_{\mathrm{LW}})$, the individual terms in Eq. (18) are approximated as

$$\frac{\partial\tilde{\mathbf{U}}}{\partial t} \approx -\frac{\omega_{\mathrm{LW}}}{2}\left[i\tilde{\mathbf{U}}_F \exp\left(-i\omega_{\mathrm{LW}}t\right) + \mathrm{c.c.}\right], \tag{A1}$$

$$\tilde{\mathbf{U}} \cdot \tilde{\nabla}\tilde{\mathbf{U}} \approx \frac{1}{4}\tilde{\nabla}\left(\tilde{\mathbf{U}}_F \cdot \tilde{\mathbf{U}}_F^*\right) - \frac{1}{4}\left(\tilde{\mathbf{U}}_F \times \tilde{\nabla} \times \tilde{\mathbf{U}}_F^* + \mathrm{c.c.}\right), \tag{A2}$$

$$\mathbf{A} \cdot \mathbf{A} \approx \frac{1}{2}\mathbf{a}_0 \cdot \mathbf{a}_0^*, \tag{A3}$$

$$\tilde{\mathbf{U}} \cdot \mathbf{A} \approx \frac{1}{4}\left\{\tilde{\mathbf{U}}_F^* \cdot \mathbf{a}_0 \exp\left[-i\left(\omega_0 - \omega_{\mathrm{LW}}\right)t\right] + \mathrm{c.c.}\right\}, \tag{A4}$$

$$\mathbf{A} \times \tilde{\nabla} \times \tilde{\mathbf{U}}$$

$$\approx \frac{1}{4}\left\{\mathbf{a}_0 \times \tilde{\nabla} \times \tilde{\mathbf{U}}_F^* \exp\left[-i\left(\omega_0 - \omega_{\mathrm{LW}}\right)t\right] + \mathrm{c.c.}\right\}, \tag{A5}$$

$$\mathbf{A} \cdot \tilde{\nabla}\tilde{\mathbf{U}}$$

$$\approx \frac{1}{4}\left\{\mathbf{a}_0 \cdot \tilde{\nabla}\tilde{\mathbf{U}}_F^* \exp\left[-i\left(\omega_0 - \omega_{\mathrm{LW}}\right)t\right] + \mathrm{c.c.}\right\}, \tag{A6}$$

where it has been assumed that $\left|\partial\tilde{\mathbf{U}}_F/\partial t\right| \ll \omega_{\mathrm{LW}}\left|\tilde{\mathbf{U}}_F\right|$ and $\left|\mathbf{U}_S\right| \ll \left|\mathbf{U}_F\right|$. Substituting these approximations in Eqs. (A1)–(A6) into Eq. (18), neglecting the second-order convective term $\tilde{\mathbf{U}} \cdot \tilde{\nabla}\tilde{\mathbf{U}}$, and collecting terms of similar frequencies, one obtains

$$\tilde{\mathbf{U}}_F = \frac{q}{im\omega_{\mathrm{LW}}}\tilde{\nabla}\left[\phi_F - \frac{1}{2c}\tilde{\mathbf{U}}_F^* \cdot \mathbf{a}_0 \exp(-i\Delta\omega t)\right]$$

$$+ \frac{q\exp(-i\Delta\omega t)}{2imc\omega_{\mathrm{LW}}}\left(\mathbf{a}_0 \times \tilde{\nabla} \times \tilde{\mathbf{U}}_F^* + \mathbf{a}_0 \cdot \tilde{\nabla}\tilde{\mathbf{U}}_F^*\right), \tag{A7}$$

and

$$\frac{1}{4}\tilde{\nabla}\left(\tilde{\mathbf{U}}_F \cdot \tilde{\mathbf{U}}_F^*\right) = \frac{1}{4}\left[\tilde{\mathbf{U}}_F \times \tilde{\nabla} \times \tilde{\mathbf{U}}_F^* + \tilde{\mathbf{U}}_F^* \times \tilde{\nabla} \times \tilde{\mathbf{U}}_F\right]$$

$$-\frac{q}{m}\tilde{\nabla}\phi_S - \frac{\tilde{\nabla}p_S}{n_S m} - \frac{q^2}{4m^2c^2}\tilde{\nabla}\left(\mathbf{a}_0 \cdot \mathbf{a}_0^*\right), \tag{A8}$$

where $\Delta\omega \equiv \omega_0 - 2\omega_{\mathrm{LW}}$. Setting $q = -e$ and $m = m_{\mathrm{e}}$, Eq. (A7) is solved approximately to give

$$\tilde{\mathbf{U}}_F \approx \frac{e}{im_{\mathrm{e}}\omega_{\mathrm{LW}}}\mathbf{E}_{\mathrm{eff}}, \tag{A9}$$

where $\mathbf{E}_{\mathrm{eff}}$ was previously defined in Eq. (28). Substituting Eq. (A9) into Eq. (A8), neglecting the term in the square brackets on the right-hand side (rhs) of Eq. (A8) and integrating the resulting equation, assuming a pressure profile $p_S = n_0 T_{\mathrm{e}0}\left(n_S/n_0\right)^{\gamma}$, with γ being the ratio of specific heats (isothermal electrons: $\gamma = 1$; adiabatic electrons: $\gamma = 5/3$), one obtains the electron equation of state, Eq. (26). This provides closure for the RPIC model.

2. Field Equations

The driving current **J** resulting from self-consistent electron motion is

$$\begin{aligned}\mathbf{J} &= -en\mathbf{U}\,,\\ &= -en\left(\tilde{\mathbf{U}} - \frac{q\mathbf{A}}{mc}\right),\\ &= -en\left(\tilde{\mathbf{U}} + \frac{e\mathbf{A}}{m_\mathrm{e}c}\right).\end{aligned}$$

The components of **J** with frequencies $\pm\omega_0$ and $\pm 2\omega_\mathrm{LW}$ (since $\omega_0 \approx 2\omega_\mathrm{LW}$ for TPD) are of importance:

$$\mathbf{J} \approx -\frac{1}{2}\left\{\left[\frac{e^2 n_{\mathrm{e}S}\mathbf{a}_0}{m_\mathrm{e}c} + \frac{en_{\mathrm{e}F}\tilde{\mathbf{U}}_F}{2}\exp\left(i\Delta\omega\tilde{t}\right)\right]\exp\left(-i\omega_0\tilde{t}\right) + \mathrm{c.c.}\right\},$$

$$\mathbf{J} \equiv \frac{1}{2}\left[\mathbf{J}_0\exp\left(-i\omega_0\tilde{t}\right) + \mathrm{c.c.}\right], \tag{A10}$$

$$\mathbf{J}_0 = -\left[\frac{e^2 n_{\mathrm{e}S}\mathbf{a}_0}{m_\mathrm{e}c} + \frac{en_{\mathrm{e}F}\tilde{\mathbf{U}}_F}{2}\exp\left(i\Delta\omega\tilde{t}\right)\right],$$

where $\tilde{\mathbf{U}}_F$ is given in Eq. (A9). On substituting Eq. (A9) into Eq. (A10), an equation for $\mathbf{J}_0$ is obtained [Eq. (33)], from which the transverse current $\mathbf{J}_{0T}$ can be computed:

$$\mathbf{J}_{0T} \equiv \mathbf{J}_0 + \tilde{\nabla}\chi_0\,,$$

$$\tilde{\nabla}^2\chi_0 = -\tilde{\nabla}\cdot\mathbf{J}_0\,,$$

$$-\frac{1}{c^2}\frac{\partial^2\mathbf{A}}{\partial t^2} + \tilde{\nabla}^2\mathbf{A} = -\frac{4\pi}{c}\frac{1}{2}\left[\mathbf{J}_{0T}\exp\left(-i\omega_0\tilde{t}\right) + \mathrm{c.c.}\right]. \tag{A11}$$

A substitution of the above expression for $\mathbf{J}_T$ into the second-order wave equation, assuming slowly varying envelopes and separating frequency components, results in a nonlinear Schrödinger equation for the evolution of the incident EM-wave envelope [Eq. (31)].

3. Time-Averaged Single-Particle Equations of Motion

The exact single-particle equation of motion is time averaged to obtain the RPIC single-particle equation of motion. Recall that Eq. (16) is exact and is applicable to both electrons and ions.

The electron particle velocity can be conveniently cast in the form

$$\tilde{\mathbf{u}}_e = \tilde{\mathbf{u}}_{e0} + \tilde{\mathbf{u}}_{\mathrm{eS}} + \frac{1}{2}\left[\tilde{\mathbf{u}}_{\mathrm{e}F}\exp\left(-i\omega_\mathrm{LW}\tilde{t}\right) + \mathrm{c.c.}\right], \tag{A12}$$

where $\tilde{\mathbf{u}}_{\mathrm{e}0}$ is the initial electron velocity, $\tilde{\mathbf{u}}_{\mathrm{e}S}$ the low-frequency velocity perturbation, and $\tilde{\mathbf{u}}_{\mathrm{e}F}$ is the high-frequency velocity perturbation. Equation (16) is solved approximately as follows: First, neglecting contributions from the laser pump and assuming $\left|\partial\tilde{\mathbf{u}}_{\mathrm{e}S}/\partial\tilde{t}\right| \ll \omega_\mathrm{LW}\left|\tilde{\mathbf{u}}_{\mathrm{e}F}\right|$, Eq. (16) yields

$$\begin{aligned}\tilde{\mathbf{u}}_{\mathrm{e}F} &\approx -\frac{e}{im_\mathrm{e}\omega_\mathrm{LW}}\tilde{\nabla}\phi_F\,,\\ &= \frac{e}{im_\mathrm{e}\omega_\mathrm{LW}}\mathbf{E}_F\,.\end{aligned}$$

Then, substituting the above approximate expression for $\tilde{\mathbf{u}}_{\mathrm{e}F}$ into Eqs. (A12) and (16) and keeping only electron responses at the ion-acoustic and Langmuir time scales, i.e., $\omega \sim 0$, $\pm\omega_\mathrm{LW}$, $\pm(\omega_0 - \omega_\mathrm{LW})$, Eq. (19) is obtained, the electron reduced-description equation of motion in the oscillating frame.

Specifying these results to 2-D, assuming polarization in the y direction and a fixed pump wave $a_0 = a_{00}\exp\left(ik_0x\right)$, Eq. (19) further reduces to give

$$\begin{aligned}m_\mathrm{e}\frac{\mathrm{d}\tilde{\mathbf{u}}_\mathrm{e}}{\mathrm{d}\tilde{t}} &\approx -e\mathbf{E} - \frac{e^2}{4m_\mathrm{e}c^2}\tilde{\nabla}\left|\mathbf{a}_0\right|^2\\ &+ \hat{\mathbf{x}}\frac{e^2k_0}{4cm_\mathrm{e}\omega_\mathrm{LW}}\left\{\mathbf{a}_0\cdot\mathbf{E}_F^*\exp\left[-i\left(\omega_0 - \omega_\mathrm{LW}\right)\tilde{t}\right] + \mathrm{c.c.}\right\}.\end{aligned} \tag{A13}$$

The ion-particle equations of motion follow similarly to yield Eq. (21).

Appendix B: Derivation of the Zakharov Equations from RPIC

In this Appendix, it will be shown how the Zakharov equations may be obtained from the RPIC model under certain approximations. This connection ensures that the RPIC equations have the correct limiting form (since the Zakharov equations may also be shown to be a consequence of the Vlasov equations on which the RPIC model is based), and that the Zakharov and RPIC models predict the same physical behavior in the linear regime.

It is noted that while the RPIC equations are more conveniently written in the oscillating frame, the Zakharov equations are customarily written in the laboratory frame of reference. To begin, Eq. (19) is transformed back into the laboratory frame of reference:

$$
\begin{aligned}
m_{\mathrm{e}}\frac{\mathrm{d}\tilde{\mathbf{u}}_{\mathrm{e}}}{\mathrm{d}t} &\approx -e\mathbf{E}-\frac{e^2}{4m_{\mathrm{e}}c^2}\nabla\left|\mathbf{a}_0\right|^2 \\
&-\frac{e^2}{4cm_{\mathrm{e}}\omega_{\mathrm{LW}}}\left[i\nabla\left(\mathbf{E}_F^*\cdot\mathbf{a}_0\right)\exp(-i\Delta\omega t)\exp\left(-i\omega_{\mathrm{LW}}t\right)+\mathrm{c.c.}\right] \\
&-\frac{e^2}{4cm_{\mathrm{e}}\omega_{\mathrm{LW}}}\Big[-i\left(\mathbf{a}_0\cdot\nabla\right)\mathbf{E}_F^*\exp(-i\Delta\omega t) \\
&\times\exp\left(-i\omega_{\mathrm{LW}}t\right)+\mathrm{c.c.}\Big],
\end{aligned}
\tag{B1}
$$

since $\tilde{\nabla}=\tilde{\nabla}$, $\tilde{t}=t$, and $\mathrm{d}/\mathrm{d}\tilde{t}=\mathrm{d}/\mathrm{d}t$, as shown previously. Here, $\mathbf{E}$ is the physical electric field reconstituted from the envelope representation

$$
\mathbf{E}=\mathbf{E}_s+\frac{1}{2}\left[\mathbf{E}_1\exp\left(-i\omega_{\mathrm{LW}}t\right)+\mathbf{E}_2\exp\left(-2i\omega_{\mathrm{LW}}t\right)+\mathrm{c.c.}\right].
\tag{B2}
$$

Using the definition $\mathbf{u}_{\mathrm{e}}=\tilde{\mathbf{u}}_{\mathrm{e}}+e\mathbf{A}/m_{\mathrm{e}}c$, one obtains from Eq. (B1)

$$
\begin{aligned}
\frac{\mathrm{d}\mathbf{u}_{\mathrm{e}}}{\mathrm{d}t} &= -\frac{e\mathbf{E}}{m_{\mathrm{e}}}-\frac{e^2\nabla\left|\mathbf{a}_0\right|^2}{4m_{\mathrm{e}}^2c^2}+\frac{e^2}{4m_{\mathrm{e}}^2c^2}\left(\mathbf{a}_0^*\cdot\nabla\mathbf{a}_0+\mathrm{c.c.}\right) \\
&-\frac{e^2}{4m_{\mathrm{e}}^2c\omega_{\mathrm{LW}}}\Big\{\Big[\nabla\left(\mathbf{E}_F^*\cdot\mathbf{a}_0\right)-\mathbf{a}_0\cdot\nabla\mathbf{E}_F^* \\
&-\mathbf{E}_F^*\cdot\nabla\mathbf{a}_0\Big]i\exp\left[-i\left(\omega_{\mathrm{LW}}+\Delta\omega\right)t\right]+\mathrm{c.c.}\Big\} \\
&-\frac{e}{m_{\mathrm{e}}}\frac{\omega_0}{2c}\left\{i\mathbf{a}_0\exp\left[-i\left(2\omega_{\mathrm{LW}}+\Delta\omega\right)t\right]+\mathrm{c.c.}\right\}.
\end{aligned}
$$

Changing to conventional Zakharov nomenclature, $\mathbf{E}_1\equiv\mathbf{E}_F$ and $\mathbf{E}_2\equiv i\omega_0\mathbf{a}_0/c$, the above equation becomes

$$
\frac{\mathrm{d}\mathbf{u}_{\mathrm{e}}}{\mathrm{d}t}=\mathcal{A},
\tag{B3}
$$

$$
\begin{aligned}
\mathcal{A} &\equiv \mathcal{A}_0+\frac{1}{2}\left[\mathcal{A}_1\exp\left(-i\omega_{\mathrm{LW}}t\right)+\mathrm{c.c.}\right] \\
&+\frac{1}{2}\left[\mathcal{A}_2\exp\left(-2i\omega_{\mathrm{LW}}t\right)+\mathrm{c.c.}\right],
\end{aligned}
\tag{B4}
$$

$$
\begin{aligned}
\mathcal{A}_0 &= -\frac{e\mathbf{E}_S}{m_{\mathrm{e}}}-\frac{e^2}{4m_{\mathrm{e}}^2\omega_0^2}\nabla\left|\mathbf{E}_2\right|^2 \\
&+\frac{e^2}{4m_{\mathrm{e}}^2\omega_0^2}\left(\mathbf{E}_2^*\cdot\nabla\mathbf{E}_2+\mathrm{c.c.}\right),
\end{aligned}
\tag{B5}
$$

$$
\begin{aligned}
\mathcal{A}_1 &= -\frac{e\mathbf{E}_1}{2m_{\mathrm{e}}} \\
&-\frac{e^2}{2m_{\mathrm{e}}^2\omega_0\omega_{\mathrm{LW}}}\Big[\nabla\left(\mathbf{E}_1^*\cdot\mathbf{E}_2\right)-\mathbf{E}_2\cdot\nabla\mathbf{E}_1^* \\
&-\mathbf{E}_1^*\cdot\nabla\mathbf{E}_2\Big]\exp(-i\Delta\omega t),
\end{aligned}
\tag{B6}
$$

$$
\mathcal{A}_2=-\frac{e\mathbf{E}_2}{2m_{\mathrm{e}}}\exp(-i\Delta\omega t),
\tag{B7}
$$

where $\Delta\omega$ was defined previously [see Eq. (30)]. The Vlasov equation corresponding to the acceleration $\mathcal{A}$ is

$$
\left(\partial_t+\mathbf{v}\cdot\partial_{\mathbf{x}}\right)F+\mathcal{A}\cdot\partial_{\mathbf{v}}F=0,
\tag{B8}
$$

where the distribution function F can be written in terms of slowly varying envelopes

$$
\begin{aligned}
F\left(\mathbf{x},t;\mathbf{v}\right) &= f_0+\frac{1}{2}\left[f_1\exp\left(-i\omega_{\mathrm{LW}}t\right)+\mathrm{c.c.}\right] \\
&+\frac{1}{2}\left[f_2\exp\left(-2i\omega_{\mathrm{LW}}t\right)+\mathrm{c.c.}\right],
\end{aligned}
\tag{B9}
$$

$$f_0(\mathbf{x},t;\mathbf{v}) = f_M(\mathbf{v}) + \delta f_0(\mathbf{x},t;\mathbf{v}) . \tag{B10}$$

Here, $f_M(\mathbf{v})$ is the time-stationary, spatially uniform background Maxwellian distribution. Substituting Eqs. (B4)–(B7) and (B9)–(B10) into Eq. (B8) and separating frequency components, one obtains the coupled equations

$$\begin{aligned}&(\partial_t + \mathbf{v}\cdot\partial_{\mathbf{x}})\delta f_0 = \frac{e}{m_\mathrm{e}}\mathbf{E}_s\cdot\partial_{\mathbf{v}}(f_M+\delta f_0)\\&+\frac{e}{4m_\mathrm{e}}\left(\mathbf{E}_1\cdot\partial_{\mathbf{v}}f_1^* + \text{c.c.}\right) + \frac{e}{4m_\mathrm{e}}\left(\tilde{\mathbf{E}}_2\cdot\partial_{\mathbf{v}}f_2^* + \text{c.c.}\right),\end{aligned}\tag{B11}$$

$$\begin{aligned}&\left(-i\omega_\mathrm{LW} + \partial_t + \mathbf{v}\cdot\partial_{\mathbf{x}}\right)f_1 = \frac{e}{m_\mathrm{e}}\left(\mathbf{E}_1+\mathbf{h}_1\right)\cdot\partial_{\mathbf{v}}\left(f_M+\delta f_0\right)\\&+\frac{e}{m_\mathrm{e}}\mathbf{E}_s\cdot\partial_{\mathbf{v}}f_1 + \frac{e}{2m_\mathrm{e}}\tilde{\mathbf{E}}_2\cdot\partial_{\mathbf{v}}f_1^* + \frac{e}{2m_\mathrm{e}}\left(\mathbf{E}_1^*+\mathbf{h}_1^*\right)\cdot\partial_{\mathbf{v}}f_2 ,\end{aligned}\tag{B12}$$

$$\begin{aligned}&\left(-2i\omega_\mathrm{LW} + \partial_t + \mathbf{v}\cdot\partial_{\mathbf{x}}\right)f_2 = \frac{e}{m_\mathrm{e}}\tilde{\mathbf{E}}_2\cdot\partial_{\mathbf{v}}\left(f_M+\delta f_0\right)\\&+\frac{e}{2m_\mathrm{e}}\left(\mathbf{E}_1+\mathbf{h}_1\right)\cdot\partial_{\mathbf{v}}f_1 + \frac{e}{m_\mathrm{e}}\mathbf{E}_s\cdot\partial_{\mathbf{v}}f_2 ,\end{aligned}\tag{B13}$$

$$\tilde{\mathbf{E}}_2 \equiv \exp(-i\Delta\omega t)\mathbf{E}_2 ,\tag{B14}$$

$$\begin{aligned}\mathbf{h}_1 \equiv \frac{e}{2m_\mathrm{e}\omega_0\omega_\mathrm{LW}}&\Big[\nabla\left(\mathbf{E}_1^*\cdot\tilde{\mathbf{E}}_2\right)\\&-\tilde{\mathbf{E}}_2\cdot\nabla\mathbf{E}_1^* - \mathbf{E}_1^*\cdot\nabla\tilde{\mathbf{E}}_2\Big],\end{aligned}\tag{B15}$$

where terms that are not linear in $\mathbf{E}_1$ or linear in $\mathbf{E}_2 \cdot \mathbf{E}_1^*$ are neglected since only the linear parametric dispersion is of interest.

Fourier transforming Eqs. (B11)–(B13) in space and time, one obtains

$$\begin{aligned}&-i(\omega-\mathbf{k}\cdot\mathbf{v})\delta f_0(\mathbf{k},\omega,\mathbf{v}) = \frac{e}{m_\mathrm{e}}\iint \mathrm{d}\mathbf{k}'\mathrm{d}\omega'\mathbf{E}_s'\cdot\partial_{\mathbf{v}}\delta f_0''\\&+\frac{e}{4m_\mathrm{e}}\iint \mathrm{d}\mathbf{k}'\mathrm{d}\omega'\mathbf{E}_1'\cdot\partial_{\mathbf{v}}\left[f_1^*\right]'' + \text{c.c.}\\&+\frac{e}{4m_\mathrm{e}}\iint \mathrm{d}\mathbf{k}'\mathrm{d}\omega'\mathbf{E}_2'\cdot\partial_{\mathbf{v}}\left[f_2^*\right]'' + \text{c.c.},\end{aligned}\tag{B16}$$

$$\begin{aligned}&-i\left(\omega_\mathrm{LW}+\omega-\mathbf{k}\cdot\mathbf{v}\right)f_1(\mathbf{k},\omega,\mathbf{v})\\&=\frac{e}{m_\mathrm{e}}\left[\mathbf{E}_1(\mathbf{k},\omega)+\mathbf{h}_1(\mathbf{k},\omega)\right]\cdot\partial_{\mathbf{v}}f_M(\mathbf{v})\\&+\frac{e}{m_\mathrm{e}}\iint \mathrm{d}\mathbf{k}'\mathrm{d}\omega'\mathbf{E}_s'\cdot\partial_{\mathbf{v}}f_1''\\&+\frac{e}{m_\mathrm{e}}\iint \mathrm{d}\mathbf{k}'\mathrm{d}\omega'\mathbf{E}_1'\cdot\partial_{\mathbf{v}}\delta f_0''\\&+\frac{e}{2m_\mathrm{e}}\iint \mathrm{d}\mathbf{k}'\mathrm{d}\omega'\tilde{\mathbf{E}}_2'\cdot\left[\partial_{\mathbf{v}}f_1^*\right]''\\&+\frac{e}{2m_\mathrm{e}}\iint \mathrm{d}\mathbf{k}'\mathrm{d}\omega'\left[\mathbf{E}_1^*\right]'\cdot\partial_{\mathbf{v}}f_2'',\end{aligned}\tag{B17}$$

$$\begin{aligned}&-i\left(2\omega_\mathrm{LW}+\omega-\mathbf{k}\cdot\mathbf{v}\right)f_2(\mathbf{k},\omega,\mathbf{v}) = \frac{e}{m_\mathrm{e}}\tilde{\mathbf{E}}_2(\mathbf{k},\omega)\cdot\partial_{\mathbf{v}}f_M(\mathbf{v})\\&+\frac{e}{m_\mathrm{e}}\iint \mathrm{d}\mathbf{k}'\mathrm{d}\omega'\mathbf{E}_2'\cdot\partial_{\mathbf{v}}\delta f_0''\\&+\frac{e}{2m_\mathrm{e}}\iint \mathrm{d}\mathbf{k}'\mathrm{d}\omega'\left(\mathbf{E}_1'+h_1'\right)\cdot\partial_{\mathbf{v}}f_1''\\&+\frac{e}{m_\mathrm{e}}\iint \mathrm{d}\mathbf{k}'\mathrm{d}\omega'\mathbf{E}_s'\cdot\partial_{\mathbf{v}}f_2'',\end{aligned}\tag{B18}$$

where

$$\begin{aligned}\tilde{\mathbf{E}}_2' &\equiv \tilde{\mathbf{E}}_2(\mathbf{k}',\omega'),\\\left[\tilde{\mathbf{E}}_1^*\right]' &\equiv \left[\tilde{\mathbf{E}}_1(-\mathbf{k}',-\omega')\right]^*,\\f_2'' &\equiv f_2(\mathbf{k}-\mathbf{k}',\omega-\omega',\mathbf{v}),\\\left[f_1^*\right]'' &\equiv \left[f_1(\mathbf{k}-\mathbf{k}',\omega-\omega',\mathbf{v})\right]^* .\end{aligned}$$

Equations (B16)–(B18) can be solved approximately. First, retaining only first-order terms in the electric fields $\mathbf{E}_1$ and $\mathbf{E}_2$, Eqs. (B16)–(B18) give

$$\delta f_0(\mathbf{k},\omega,\mathbf{v}) = \frac{e}{m_\mathrm{e}}\frac{\mathbf{E}_s(\mathbf{k},\omega)\cdot\partial_{\mathbf{v}}f_M(\mathbf{v})}{-i(\omega-\mathbf{k}\cdot\mathbf{v})} ,\tag{B19}$$

$$f_1(\mathbf{k},\omega,\mathbf{v}) = \frac{e}{m_\mathrm{e}}\,\frac{\mathbf{E}_1(\mathbf{k},\omega)\cdot\partial_\mathbf{v} f_M(\mathbf{v})}{-i(\omega_\mathrm{LW}+\omega-\mathbf{k}\cdot\mathbf{v})}, \tag{B20}$$

$$f_2(\mathbf{k},\omega,\mathbf{v}) = \frac{e}{m_\mathrm{e}}\,\frac{\tilde{\mathbf{E}}_2(\mathbf{k},\omega)\cdot\partial_\mathbf{v} f_M(\mathbf{v})}{-i(2\omega_\mathrm{LW}+\omega-\mathbf{k}\cdot\mathbf{v})}. \tag{B21}$$

Substituting the above approximate expressions for $\delta f_0(\mathbf{k},\omega,\mathbf{v})$, $f_1(\mathbf{k},\omega,\mathbf{v})$, and $f_2(\mathbf{k},\omega,\mathbf{v})$ into the right-hand side (rhs) of Eq. (B17), one obtains

$$\begin{aligned}
f_1(\mathbf{k},\omega,\mathbf{v}) &= \frac{e}{m_\mathrm{e}}\,\frac{\left[\mathbf{E}_1(\mathbf{k},\omega)+\mathbf{h}_1(\mathbf{k},\omega)\right]\cdot\partial_\mathbf{v} f_0(\mathbf{v})}{-i(\omega_\mathrm{LW}+\omega-\mathbf{k}\cdot\mathbf{v})}\\
&-\frac{e^2}{m_\mathrm{e}}\,\frac{1}{(\omega_\mathrm{LW}+\omega-\mathbf{k}\cdot\mathbf{v})}\\
&\times\iint \mathrm{d}\mathbf{k}'\mathrm{d}\omega'\,\mathbf{E}_s(\mathbf{k}',\omega')\cdot\partial_\mathbf{v}\left[\frac{\mathbf{E}_1(\mathbf{k}'-\mathbf{k},\omega'-\omega)\cdot\partial_\mathbf{v} f_M}{\left[\omega_\mathrm{LW}+\omega'-\omega-(\mathbf{k}'-\mathbf{k})\cdot\mathbf{v}\right]}\right]\\
&-\frac{e^2}{2m_\mathrm{e}^2}\,\frac{1}{(\omega_\mathrm{LW}+\omega-\mathbf{k}\cdot\mathbf{v})}\\
&\times\iint \mathrm{d}\mathbf{k}'\mathrm{d}\omega'\,\mathbf{E}_1(\mathbf{k}',\omega')\cdot\partial_\mathbf{v}\left[\frac{\mathbf{E}_s(\mathbf{k}'-\mathbf{k},\omega'-\omega)\cdot\partial_\mathbf{v} f_M}{\left[\omega'-\omega-(\mathbf{k}'-\mathbf{k})\cdot\mathbf{v}\right]}\right]\\
&+\frac{e^2}{2m_\mathrm{e}^2}\,\frac{1}{(\omega_\mathrm{LW}+\omega-\mathbf{k}\cdot\mathbf{v})}\\
&\times\iint \mathrm{d}\mathbf{k}'\mathrm{d}\omega'\,\tilde{\mathbf{E}}_2(\mathbf{k}',\omega')\cdot\partial_\mathbf{v}\left[\frac{\mathbf{E}_1^*(\mathbf{k}'-\mathbf{k},\omega'-\omega)\cdot\partial_\mathbf{v} f_M}{\left[\omega_\mathrm{LW}+\omega'-\omega-(\mathbf{k}'-\mathbf{k})\cdot\mathbf{v}\right]}\right]\\
&-\frac{e^2}{2m_\mathrm{e}^2}\,\frac{1}{(\omega_\mathrm{LW}+\omega-\mathbf{k}\cdot\mathbf{v})}\\
&\times\iint \mathrm{d}\mathbf{k}'\mathrm{d}\omega'\,\mathbf{E}_1^*(-\mathbf{k}',-\omega')\\
&\cdot\partial_\mathbf{v}\left[\frac{\tilde{\mathbf{E}}_2(\mathbf{k}-\mathbf{k}',\omega-\omega')\cdot\partial_\mathbf{v} f_M}{\left[2\omega_\mathrm{LW}+\omega-\omega'-(\mathbf{k}-\mathbf{k}')\cdot\mathbf{v}\right]}\right].
\end{aligned} \tag{B22}$$

In order to solve Eq. (B22), $\mathbf{E}_1(\mathbf{k},\omega)$ must first be computed. The Poisson equation, in conjunction with the continuity equation and the gauge condition $\nabla\cdot\mathbf{A}=0$, gives

$$\mathbf{k}\cdot\mathbf{E}_1(\mathbf{k},\omega) = \frac{4\pi\mathbf{k}\cdot\mathbf{J}_1(\mathbf{k},\omega)}{i\omega_\mathrm{LW}}, \tag{B23}$$

$$\mathbf{J}_1(\mathbf{k},\omega) = -e\int \mathrm{d}^3\mathbf{v}\,\mathbf{v}f_1(\mathbf{k},\omega,\mathbf{v}), \tag{B24}$$

where, consistent with the envelope approximation, $|\omega| \ll \omega_\mathrm{LW}$.

Substituting Eq. (B22) into Eq. (B24) leads to

$$\mathbf{J}_1 = \mathbf{J}_1^0 + \delta\mathbf{J}_1^0 + \delta\mathbf{J}_1^1 + \delta\mathbf{J}_1^2, \tag{B25}$$

$$\mathbf{J}_1^0 = \frac{e^2}{m_\mathrm{e}}\int \mathrm{d}^3\mathbf{v}\left[\frac{\mathbf{v}\mathbf{E}_1(\mathbf{k},\omega)\cdot\partial_\mathbf{v} f_0}{i(\omega_\mathrm{LW}+\omega-\mathbf{k}\cdot\mathbf{v})}\right], \tag{B26}$$

$$\begin{aligned}
\delta\mathbf{J}_1^0 &= \frac{e^2}{m_\mathrm{e}}\int \mathrm{d}^3\mathbf{v}\left[\frac{\mathbf{v}\mathbf{h}_1(\mathbf{k},\omega)\cdot\partial_\mathbf{v} f_0}{i(\omega_\mathrm{LW}+\omega-\mathbf{k}\cdot\mathbf{v})}\right]\\
&+\frac{e^3}{m_\mathrm{e}^2}\int \mathrm{d}\mathbf{k}'\int \mathrm{d}\omega'\int \mathrm{d}^3\mathbf{v}\,\frac{\mathbf{v}\mathbf{E}_s(\mathbf{k}',\omega')}{(\omega_\mathrm{LW}+\omega-\mathbf{k}\cdot\mathbf{v})}\\
&\cdot\partial_\mathbf{v}\left[\frac{\mathbf{E}_1(\mathbf{k}'-\mathbf{k},\omega'-\omega)\cdot\partial_\mathbf{v} f_M}{\left[\omega_\mathrm{LW}+\omega'-\omega-(\mathbf{k}'-\mathbf{k})\cdot\mathbf{v}\right]}\right]\\
&+\frac{e^3}{m_\mathrm{e}^2}\int \mathrm{d}\mathbf{k}'\int \mathrm{d}\omega'\int \mathrm{d}^3\mathbf{v}\,\frac{\mathbf{v}\mathbf{E}_1(\mathbf{k}',\omega')}{(\omega_\mathrm{LW}+\omega-\mathbf{k}\cdot\mathbf{v})}\\
&\cdot\partial_\mathbf{v}\left[\frac{\mathbf{E}_s(\mathbf{k}'-\mathbf{k},\omega'-\omega)\cdot\partial_\mathbf{v} f_M}{\left[\omega'-\omega-(\mathbf{k}'-\mathbf{k})\cdot\mathbf{v}\right]}\right],
\end{aligned} \tag{B27}$$

$$\begin{aligned}
\delta\mathbf{J}_1^1 &= -\frac{e^3}{2m_\mathrm{e}^2}\int \mathrm{d}\mathbf{k}'\int \mathrm{d}\omega'\int \mathrm{d}^3\mathbf{v}\,\frac{\mathbf{v}\tilde{\mathbf{E}}_2(\mathbf{k}',\omega')}{(\omega_\mathrm{LW}+\omega-\mathbf{k}\cdot\mathbf{v})}\\
&\cdot\partial_\mathbf{v}\left[\frac{\mathbf{E}_1^*(\mathbf{k}'-\mathbf{k},\omega'-\omega)\cdot\partial_\mathbf{v} f_0}{\omega_\mathrm{LW}+\omega'-\omega-(\mathbf{k}'-\mathbf{k})\cdot\mathbf{v}}\right],
\end{aligned} \tag{B28}$$

$$\delta\mathbf{J}_1^2 = \frac{e^3}{2m_\mathrm{e}^2}\int \mathrm{d}\mathbf{k}'\int \mathrm{d}\omega'\int \mathrm{d}^3\mathbf{v}\,\frac{\mathbf{v}\mathbf{E}_1^*(-\mathbf{k}',-\omega')}{(\omega_\mathrm{LW}+\omega-\mathbf{k}\cdot\mathbf{v})}$$

$$\cdot\partial_\mathbf{v}\left[\frac{\tilde{\mathbf{E}}_2(\mathbf{k}-\mathbf{k}',\omega-\omega')\cdot\partial_\mathbf{v}f_0}{2\omega_\mathrm{LW}+\omega-\omega'-(\mathbf{k}-\mathbf{k}')\cdot\mathbf{v}}\right]. \tag{B29}$$

Note that since $\mathbf{E}_1$ is a longitudinal field,

$$\mathbf{E}_1(\mathbf{k},\omega) = \frac{\mathbf{k}[\mathbf{k}\cdot\mathbf{E}_1(\mathbf{k},\omega)]}{k^2}. \tag{B30}$$

Equation (B26) is evaluated, using the approximation $|\omega| \ll \omega_\mathrm{LW}$ to give

$$\frac{4\pi\mathbf{k}\cdot\mathbf{J}_1^0}{i\omega_\mathrm{LW}} = -\chi_e(\mathbf{k},\omega+\omega_\mathrm{LW})\mathbf{k}\cdot\mathbf{E}_1(\mathbf{k},\omega), \tag{B31}$$

where

$$\chi_e(\mathbf{k},\omega) \equiv \frac{4\pi e^2}{m_\mathrm{e}k^2}\int \mathrm{d}^3\mathbf{v}\left[\frac{\mathbf{k}\cdot\partial_\mathbf{v}f_0}{\omega-\mathbf{k}\cdot\mathbf{v}}\right].$$

Equation (B27) is evaluated similarly to yield

$$\frac{4\pi\mathbf{k}\cdot\delta\mathbf{J}_1^0(\mathbf{k},\omega)}{i\omega_\mathrm{LW}} = -\chi_\mathrm{e}(\mathbf{k},\omega+\omega_\mathrm{LW})\mathbf{k}\cdot\mathbf{h}_1(\mathbf{k},\omega)$$

$$+\,i\int \mathrm{d}\mathbf{k}'\int \mathrm{d}\omega'\left[\mathbf{k}\cdot\mathbf{E}_1(\mathbf{k}',\omega')\,\frac{\delta n_{\mathrm{e}S}(\mathbf{k}'-\mathbf{k},\omega'-\omega)}{n_\mathrm{e0}}\right]. \tag{B32}$$

To obtain the right-hand side of Eq. (B32), it was assumed that $|\omega|,|\omega'| \ll \omega_\mathrm{LW}$,

$$|\omega'-\omega| \le |\mathbf{k}'-\mathbf{k}|c_s \ll |(\mathbf{k}'-\mathbf{k})\cdot\mathbf{v}| \sim |\mathbf{k}'-\mathbf{k}|v_\mathrm{the},$$

and the relation

$$\delta n_{\mathrm{e}S}(\mathbf{k},\omega) = -e\phi_{\mathrm{e}S}(\mathbf{k},\omega)/T_\mathrm{e0},$$

where $\mathbf{E}_s(\mathbf{k},\omega) = -i\mathbf{k}\phi_{\mathrm{e}S}(\mathbf{k},\omega)$ was used.

Using the approximations $|\omega-\mathbf{k}\cdot\mathbf{v}| \ll \omega_\mathrm{LW}$ and

$$|\omega'-\omega-(\mathbf{k}'-\mathbf{k})\cdot\mathbf{v}| \ll \omega_\mathrm{LW},$$

neglecting smaller terms of the order $\mathbf{k}\cdot\mathbf{v}/\omega_\mathrm{LW} \sim k\lambda_\mathrm{De} \ll 1$, and applying two successive integration by parts in velocity space, Eq. (B28) is evaluated:

$$\delta\mathbf{J}_1^1(\mathbf{k},\omega)$$

$$= -\frac{e^3 n_\mathrm{e0}}{2m_\mathrm{e}^2\omega_\mathrm{LW}^3}\int \mathrm{d}\mathbf{k}'\int \mathrm{d}\omega'\left[\mathbf{E}_1^*(\mathbf{k}'-\mathbf{k},\omega'-\omega)\cdot\mathbf{k}\right]\tilde{\mathbf{E}}_2(\mathbf{k}',\omega')$$

$$-\frac{e^3 n_\mathrm{e0}}{2m_\mathrm{e}^2\omega_\mathrm{LW}^3}\int \mathrm{d}\mathbf{k}'\int \mathrm{d}\omega'\,\mathbf{E}_1^*(\mathbf{k}'-\mathbf{k},\omega'-\omega)\left[\tilde{\mathbf{E}}_2(\mathbf{k}',\omega')\cdot\mathbf{k}\right]$$

$$-\frac{e^3 n_\mathrm{e0}}{2m_\mathrm{e}^2\omega_\mathrm{LW}^3}\int \mathrm{d}\mathbf{k}'\int \mathrm{d}\omega'\,\tilde{\mathbf{E}}_2(\mathbf{k}',\omega')$$

$$\times\left[\mathbf{E}_1^*(\mathbf{k}'-\mathbf{k},\omega'-\omega)\cdot(\mathbf{k}'-\mathbf{k})\right]. \tag{B33}$$

Similarly, using the same approximations and integration by parts, Eq. (B30) is evaluated:

$$\delta\mathbf{J}_1^2(\mathbf{k},\omega)$$

$$= \frac{e^3 n_\mathrm{e0}}{4m_\mathrm{e}^2\omega_\mathrm{LW}^3}\int \mathrm{d}\mathbf{k}'\int \mathrm{d}\omega'\,\mathbf{E}_1^*(-\mathbf{k}',-\omega')\left[\tilde{\mathbf{E}}_2(\mathbf{k}-\mathbf{k}',\omega-\omega')\cdot\mathbf{k}\right]$$

$$+\frac{e^3 n_\mathrm{e0}}{4m_\mathrm{e}^2\omega_\mathrm{LW}^3}\int \mathrm{d}\mathbf{k}'\int \mathrm{d}\omega'\left[\mathbf{E}_1^*(-\mathbf{k}',-\omega')\cdot\mathbf{k}\right]$$

$$\times\,\tilde{\mathbf{E}}_2(\mathbf{k}-\mathbf{k}',\omega-\omega'). \tag{B34}$$

Equation (B34) is recast using the change of variables $\mathbf{k}'' = \mathbf{k}-\mathbf{k}'$ and $\omega'' = \omega-\omega'$:

$$\delta\mathbf{J}_1^2(\mathbf{k},\omega)$$

$$= \frac{e^3 n_{e0}}{4m_e^2\omega_{LW}^3}\int d\mathbf{k}''\int d\omega'' \mathbf{E}_1^*(\mathbf{k}''-\mathbf{k},\omega''-\omega)\left[\tilde{\mathbf{E}}_2(\mathbf{k}'',\omega'')\cdot\mathbf{k}\right]$$

$$+ \frac{e^3 n_{e0}}{4m_e^2\omega_{LW}^3}\int d\mathbf{k}''\int d\omega'' \left[\mathbf{E}_1^*(\mathbf{k}''-\mathbf{k},\omega''-\omega)\cdot\mathbf{k}\right]$$

$$\times\tilde{\mathbf{E}}_2(\mathbf{k}'',\omega''). \tag{B35}$$

Summing Eqs. (B33) and (B35), rearranging the resulting equation, and using the fact that $\tilde{\mathbf{E}}_2$ is a transverse field, i.e., $\tilde{\mathbf{E}}_2(\mathbf{k}',\omega')\cdot\mathbf{k}' = 0$, one obtains

$$\delta\mathbf{J}_1^1 + \delta\mathbf{J}_1^2$$

$$= \frac{ie^3 n_{e0}}{4m_e^2\omega_{LW}^3}\int d\mathbf{k}'\int d\omega' \left[\mathbf{E}_1^*(\mathbf{k}'-\mathbf{k},\omega'-\omega)\cdot i\mathbf{k}'\right]\tilde{\mathbf{E}}_2(\mathbf{k}',\omega')$$

$$- \frac{ie^3 n_{e0}}{4m_e^2\omega_{LW}^3}\int d\mathbf{k}'\int d\omega' \left[\mathbf{E}_1^*(\mathbf{k}'-\mathbf{k},\omega'-\omega)\cdot i(\mathbf{k}-\mathbf{k}')\right]\tilde{\mathbf{E}}_2(\mathbf{k}',\omega')$$

$$+ \frac{ie^3 n_{e0}}{4m_e^2\omega_{LW}^3}\int d\mathbf{k}'\int d\omega' \left[\tilde{\mathbf{E}}_2(\mathbf{k}',\omega')\cdot i(\mathbf{k}-\mathbf{k}')\right]$$

$$\times\mathbf{E}_1^*(\mathbf{k}'-\mathbf{k},\omega'-\omega). \tag{B36}$$

Using the approximations $\chi_e(\mathbf{k},\omega+\omega_{LW}) \approx -\omega_{pe0}^2/\omega_{LW}^2$ and $\omega_0 \sim 2\omega_{LW}$, and transforming Eq. (B32) back to configuration space with $i\mathbf{k} \longrightarrow \nabla$, results in

$$\nabla\cdot\delta\mathbf{J}_0^1 = \frac{ie^3 n_{e0}}{4m_e^2\omega_{LW}^3}\nabla\cdot\Big[\nabla\left(\mathbf{E}_1^*\cdot\tilde{\mathbf{E}}_2\right)$$

$$-\left(\tilde{\mathbf{E}}_2\cdot\nabla\right)\mathbf{E}_1^* - \left(\mathbf{E}_1^*\cdot\nabla\right)\tilde{\mathbf{E}}_2\Big]. \tag{B37}$$

Transforming Eq. (B36) back to configuration space, one obtains

$$\nabla\cdot\left(\delta\mathbf{J}_1^1+\delta\mathbf{J}_1^2\right) = \frac{ie^3 n_{e0}}{4m_e^2\omega_{LW}^3}\nabla\cdot\Big[\left(\mathbf{E}_1^*\cdot\nabla\right)\tilde{\mathbf{E}}_2$$

$$-\tilde{\mathbf{E}}_2\left(\nabla\cdot\mathbf{E}_1^*\right) - \left(\tilde{\mathbf{E}}_2\cdot\nabla\right)\mathbf{E}_1^*\Big]. \tag{B38}$$

Substituting Eqs. (B25), (B31), (B32), and (B36) into Eq. (B23) and transforming back to configuration space with $i\mathbf{k} \longrightarrow \nabla$, one finds

$$\mathcal{F}^{-1}\left[i\mathbf{k}\cdot\mathbf{E}_1(\mathbf{k},\omega)\epsilon\left(k,\omega+\omega_{LW}\right)\right]$$

$$+\mathcal{F}^{-1}\left\{i\int d\mathbf{k}'\int d\omega'\left[\mathbf{k}\cdot\mathbf{E}_1(\mathbf{k}',\omega')\frac{\delta n_{eS}(\mathbf{k}'-\mathbf{k},\omega'-\omega)}{n_{e0}}\right]\right\}$$

$$= \frac{e\omega_{pe0}^2}{4m_e\omega_{LW}^4}\nabla\cdot\left[\nabla\left(\mathbf{E}_1^*\cdot\tilde{\mathbf{E}}_2\right) - \tilde{\mathbf{E}}_2\left(\nabla\cdot\mathbf{E}_1^*\right)\right], \tag{B39}$$

where the operator $\mathcal{F}^{-1}$ denotes the inverse Fourier transform in space and time, and

$$\epsilon\left(\mathbf{k},\omega+\omega_{LW}\right) = 1+\chi_e\left(\mathbf{k},\omega+\omega_{LW}\right),$$

$$\approx \frac{2\omega_{pe0}\left[\omega(k)+i\gamma_L(k)\right]-3k^2v_{the}^2}{-\omega_{pe0}^2}.$$

In this approximation, Eq. (B39) can then be evaluated explicitly to yield the well-known Zakharov equation

$$\nabla\cdot\left\{\left[2i\omega_{pe0}\left(\partial_t+\gamma_L\circ\right)+3v_{the}^2\nabla^2+\omega_{pe0}^2\frac{\delta n_{eS}}{n_{e0}}\right]\mathbf{E}_1\right\}$$

$$= \frac{e}{4m_e}\nabla\cdot\left[\nabla\left(\mathbf{E}_1^*\cdot\tilde{\mathbf{E}}_2\right) - \tilde{\mathbf{E}}_2\left(\nabla\cdot\mathbf{E}_1^*\right)\right], \tag{B40}$$

where the operator "$\circ$" is used to denote a convolution in configuration space (see DuBois *et al.*[9]). The iterative procedure leading to Eq. (B22) is based on the assumption that the perturbations of the distribution function are small compared to the background distribution function f_M. This leads to the validity estimates for the Zakharov model: $\left|\mathbf{E}_1\right|^2 / 4\pi n_{\mathrm{e}0} T_{\mathrm{e}0} \ll 1$, $\left|\mathbf{E}_2\right|^2 / 4\pi n_{\mathrm{e}0} T_{\mathrm{e}0} \ll 1$, $\left|e\phi_{\mathrm{e}S} / T_{\mathrm{e}0}\right| \ll 1$, $\left|\delta n_{\mathrm{e}S} / n_{\mathrm{e}0}\right| \ll 1$, and $k_{\mathrm{LW}}\lambda_{\mathrm{De}} \ll 1$. These involve qualitative arguments, and the quantitative strengths of the inequalities are not known *a priori*. Furthermore, this derivation does not account for the evolution of the background electron-velocity distribution function, which is here taken to be a fixed Maxwellian, $f_M(v)$. This is why detailed quantitative comparison of the ZAK model with RPIC is desirable.

The equation for the low-frequency density fluctuation can be derived in a similar way. The result is

$$\left[\partial_t^2 + 2i\nu_{\mathrm{i}} \circ \partial_t - c_s^2 \nabla^2\right]\delta n = \frac{1}{16\pi m_{\mathrm{i}}} \nabla^2 \left[\left|\mathbf{E}_1\right|^2 + \frac{1}{4}\left|\mathbf{E}_2\right|^2\right]. \tag{B41}$$

In the simulations reported in the text where the laser is a uniform plane wave, the ponderomotive pressure of the pump [the second term on the right-hand side of Eq. (41)] does not contribute.

Appendix C: Degenerate LW's with Overlapping Beams

In the presence of two identical beams propagating at angles $\theta = \pm\theta_b$ with respect to the x axis, the locations of the most linearly unstable LW are given by algebraic solutions of the following two sets of equations:

$$\left(k_{x1}\cos\theta_b + k_{y1}\sin\theta_b - \frac{1}{2}k_0\lambda_{\mathrm{De}}\right)^2 + \left(-k_{x1}\sin\theta_b + k_{y1}\cos\theta_b\right)^2 = \kappa^2, \tag{C1}$$

$$\left(k_{x1}\cos\theta_b + k_{y1}\sin\theta_b - \frac{1}{2}k_0\lambda_{\mathrm{De}}\right)^2 - \left(-k_{x1}\sin\theta_b + k_{y1}\cos\theta_b\right)^2 = \left(\frac{1}{2}k_0\lambda_{\mathrm{De}}\right)^2, \tag{C2}$$

$$\left(k_{x2}\cos\theta_b - k_{y2}\sin\theta_b - \frac{1}{2}k_0\lambda_{\mathrm{De}}\right)^2 + \left(k_{x2}\sin\theta_b + k_{y2}\cos\theta_b\right)^2 = \kappa^2, \tag{C3}$$

$$\left(k_{x2}\cos\theta_b - k_{y2}\sin\theta_b - \frac{1}{2}k_0\lambda_{\mathrm{De}}\right)^2 - \left(k_{x2}\sin\theta_b + k_{y2}\cos\theta_b\right)^2 = \left(\frac{1}{2}k_0\lambda_{\mathrm{De}}\right)^2, \tag{C4}$$

where κ is defined by

$$\kappa^2 \equiv \frac{1}{2}\Omega - \left(\frac{1}{2}k_0\lambda_{\mathrm{De}}\right)^2,$$

$$\Omega \equiv \frac{2}{3}\left(\frac{\omega_0}{\omega_{pe0}} - 2\right).$$

Equations (C1)–(C4) are obtained by rotating Eqs. (34) and (35) through angles $\pm\theta_b$. For arbitrary temperature $T_{\mathrm{e}0}$ and density $n_{\mathrm{e}0}$, the solutions of Eqs. (C1)–(C2) and (C3)–(C4) result in eight distinct modes since each set of circles and hyperbolae will have four distinct intersections. There exists, however, a combination of temperature and density such that two of the eight solutions become degenerate, i.e., there will be only seven distinct solutions for (k_{x1},k_{y1}) and (k_{x2},k_{y2}). By symmetry, this special condition occurs when $k_{y1} = k_{y2} = 0$, in which case the location $k_x = k_{x1} = k_{x2}$ of the degenerate mode is given by

$$\left(k_x\cos\theta_b - \frac{1}{2}k_0\lambda_{\mathrm{De}}\right)^2 + k_x^2\sin^2\theta_b = \frac{1}{3}\left(\frac{\omega_0}{\omega_{\mathrm{pe}0}} - 2\right) - \left(\frac{1}{2}k_0\lambda_{\mathrm{De}}\right)^2, \tag{C5}$$

$$\left(k_x\cos\theta_b - \frac{1}{2}k_0\lambda_{\mathrm{De}}\right)^2 - k_x^2\sin^2\theta_b = \left(\frac{1}{2}k_0\lambda_{\mathrm{De}}\right)^2. \tag{C6}$$

Equations (C5) and (C6) are augmented by the electromagnetic dispersion relation

$$\omega_0^2 = \omega_{\mathrm{pe}0}^2 + k_0^2 c^2 . \tag{C7}$$

Equations (C5)–(C7) are solved for the background electron density given by

$$\frac{n_{\mathrm{e}0}}{n_c} = 4\left[-\sigma + \left(\sigma^2 - 8\sigma + 4\right)^{1/2}\right]^{-2},$$

$$\sigma \equiv \frac{2}{3}\left[\frac{511}{T_{\mathrm{e}}(\mathrm{keV})}\right]\cos^2\left(2\theta_b\right). \tag{C8}$$

REFERENCES

1. W. Seka, D. H. Edgell, J. F. Myatt, A. V. Maximov, R. W. Short, V. N. Goncharov, and H. A. Baldis, Phys. Plasmas **16**, 052701 (2009).
2. J. A. Delettrez, V. N. Goncharov, P. B. Radha, C. Stoeckl, A. V. Maximov, T. C. Sangster, J. A. Frenje, and D. Shvarts, Bull. Am. Phys. Soc. **53**, 248 (2008).
3. V. A. Smalyuk, D. Shvarts, R. Betti, J. A. Delettrez, D. H. Edgell, V. Yu. Glebov, V. N. Goncharov, R. L. McCrory, D. D. Meyerhofer, P. B. Radha, S. P. Regan, T. C. Sangster, W. Seka, S. Skupsky, C. Stoeckl, B. Yaakobi, J. A. Frenje, C. K. Li, R. D. Petrasso, and F. H. Séguin, Phys. Rev. Lett. **100**, 185005 (2008).
4. B. Yaakobi, T. R. Boehly, T. C. Sangster, D. D. Meyerhofer, B. A. Remington, P. G. Allen, S. M. Pollaine, H. E. Lorenzana, K. T. Lorenz, and J. A. Hawreliak, Phys. Plasmas **15**, 062703 (2008).
5. M. V. Goldman, Ann. Phys. **38**, 117 (1966); C. S. Liu and M. N. Rosenbluth, Phys. Fluids **19**, 967 (1976); A. B. Langdon, B. F. Lasinski, and W. L. Kruer, Phys. Rev. Lett. **43**, 133 (1979); S. J. Karttunen, Plasma Phys. **22**, 151 (1980); A. M. Rubenchik, Sov. Phys.-JETP **41**, 498 (1975); B. Bezzerides and D. F. DuBois, Phys. Rev. Lett. **36**, 729 (1976); R. Z. Sagdeev *et al*., Sov. Phys.-JETP **55**, 74 (1982); H. H. Chen and C. S. Liu, Phys. Rev. Lett. **39**, 881 (1977); J. Meyer, Phys. Fluids B **4**, 2934 (1992).
6. A. Simon, R. W. Short, E. A. Williams, and T. Dewandre, Phys. Fluids **26**, 3107 (1983); B. B. Afeyan and E. A. Williams, Phys. Rev. Lett. **75**, 4218 (1995).
7. H. A. Baldis and C. J. Walsh, Phys. Rev. Lett. **47**, 1658 (1981); D. M. Villeneuve, H. A. Baldis, and C. J. Walsh, Phys. Fluids **28**, 1454 (1985); K. A. Tanaka, B. Boswell, R. S. Craxton, L. M. Goldman, F. Guglielmi, W. Seka, R. W. Short, and J. M. Soures, Phys. Fluids **28**, 2910 (1985); W. Seka, B. B. Afeyan, R. Boni, L. M. Goldman, R. W. Short, K. Tanaka, and T. W. Johnston, Phys. Fluids **28**, 2570 (1985); P. E. Young *et al*., Phys. Rev. Lett. **61**, 2766 (1988); W. Seka, R. E. Bahr, R. W. Short, A. Simon, R. S. Craxton, D. S. Montgomery, and A. E. Rubenchik, Phys. Fluids B **4**, 2232 (1992).
8. Hard x rays are signatures for hot-electron generation and preheat.
9. D. F. DuBois, D. A. Russell, and H. A. Rose, Phys. Rev. Lett. **74**, 3983 (1995).
10. H. X. Vu, D. F. DuBois, and B. Bezzerides, Phys. Rev. Lett. **86**, 4306 (2001); *ibid*., Phys. Plasmas **14**, 012702 (2007).
11. K. Y. Sanbonmatsu *et al*., Phys. Rev. Lett. **82**, 932 (1999); *ibid*., Phys. Plasmas **7**, 1723 (2000).
12. J. L. Kline *et al*., Phys. Rev. Lett. **94**, 175003 (2005); J. L. Kline *et al*., Phys. Plasmas **13**, 055906 (2006).
13. In point of fact, we show in Appendix B that the ZAK model can be derived from the basic equations of the RPIC model under certain conditions.
14. R. Yan *et al*., Phys. Rev. Lett. **103**, 175002 (2009).
15. H. X. Vu, B. Bezzerides, and D. F. DuBois, J. Comput. Phys. **156**, 12 (1999).
16. H. X. Vu, J. M. Wallace, and B. Bezzerides, Phys. Plasmas **1**, 3542 (1994).
17. D. A. Russell and D. F. DuBois, Phys. Rev. Lett. **86**, 428 (2001).
18. D. F. DuBois, D. A. Russell, H. X. Vu, J. F. Myatt, and W. Seka, "The Nonlinear Source for Radiation, from the Two-Plasmon-Decay Instability, at One-Half of the Laser Frequency," in preparation (2010).
19. In the absence of SRS, the vector potential envelopes $\mathbf{a}_{-1}$ and $\mathbf{a}_1$ (with carrier frequencies $\omega_0 - \omega_{\mathrm{pe}0}$ and $\omega_0 + \omega_{\mathrm{pe}0}$, respectively) are set to 0.
20. J. F. Myatt, J. A. Delettrez, W. Seka, D. H. Edgell, A. V. Maximov, R. W. Short, D. F. DuBois, D. A. Russell, and H. X. Vu, Bull. Am. Phys. Soc. **54**, 145 (2009).
21. R. W. Short, Bull. Am. Phys. Soc. **54**, 144 (2009).
22. If above the LDI threshold, a Langmuir wave with wave number $k_{\mathrm{LW}}\lambda_{\mathrm{De}}$ will decay into a pair of LW and IAW with $k_{\mathrm{LW}1}\lambda_{\mathrm{De}} = -k_{\mathrm{LW}}\lambda_{\mathrm{De}} + \Delta k\lambda_{\mathrm{De}}$ and $k_{\mathrm{IAW}1}\lambda_{\mathrm{De}} = 2\,k_{\mathrm{LW}}\lambda_{\mathrm{De}} - \Delta k\lambda_{\mathrm{De}}$, where $\Delta k\lambda_{\mathrm{De}} = 1.5\,(m_{\mathrm{e}}/m_{\mathrm{i}})^{1/2}$ (cf. Ref. 11). This process can continue where the LW resulting from the primary LDI step can result in a secondary LDI decay step. Repeated LDI decays may occur until the resulting LW's are of sufficiently long wavelengths that LW cavitation can be nucleated.[9]
23. W. L. Kruer, *The Physics of Laser–Plasma Interactions*, Frontiers in Physics, Vol. 73, edited by D. Pines (Addison-Wesley, Redwood City, CA, 1988), p. 133.™
24. The Workshop on SRS/SBS Non-Linear Saturation at Wente Vineyards, Livermore, CA, University of California Report UCRL-JC-148983-SUM (2002).